

PAPER • OPEN ACCESS

Atomic oxygen densities in parallel plate radio frequency driven He/O₂ micro-scaled atmospheric pressure plasma jets: a systematic model validation study

To cite this article: Youfan He *et al* 2025 *Plasma Sources Sci. Technol.* **34** 095018

View the [article online](#) for updates and enhancements.

You may also like

- [Atomic oxygen generation in atmospheric pressure RF plasma jets driven by tailored voltage waveforms in mixtures of He and O₂](#)
I Korolov, D Steuer, L Bischoff *et al.*
- [Local enhancement of electron heating and neutral species generation in radio-frequency micro-atmospheric pressure plasma jets: the effects of structured electrode topologies](#)
Yue Liu, Máté Vass, Gerrit Hübner *et al.*
- [Measurement of atomic oxygen densities using TALIF on a dielectric barrier discharge: insights into the volume above a micro cavity plasma array](#)
David Steuer, Brian Z Bentz, Kevin Youngman *et al.*



HIDEN
ANALYTICAL
*Trusted in Research
for over 40 years*

www.HidenAnalytical.com

Plasma Diagnostics for Fundamental and Applied Research

Mass & energy analysis of ions, neutrals and radicals

ESPion Advanced Langmuir Probe

- Langmuir probes for plasma diagnostics
- RF compensation
- Multiple configuration options available

Find Solutions for Your Research

Atomic oxygen densities in parallel plate radio frequency driven He/O₂ micro-scaled atmospheric pressure plasma jets: a systematic model validation study

Youfan He^{1,*} , Ralf Peter Brinkmann¹ , Efe Kemaneci^{1,*}  and Andrew R Gibson^{2,3,*} 

¹ Institute of Theoretical Electrical Engineering, Faculty of Electrical Engineering and Information Technology, Ruhr University Bochum, Bochum, Germany

² Research Group for Biomedical Plasma Technology, Faculty of Electrical Engineering and Information Technology, Ruhr University Bochum, Bochum, Germany

³ York Plasma Institute, School of Physics, Engineering and Technology, University of York, York, United Kingdom

E-mail: heyoufan1993@gmail.com, efekemaneci@gmail.com and andrew.gibson@york.ac.uk

Received 1 February 2025, revised 22 July 2025

Accepted for publication 27 August 2025

Published 30 September 2025



Abstract

Reactive species produced by atmospheric pressure plasma jets have high application potential in the fields of biomedicine and surface processing. An extensive validation between the simulation results in this work and measurement data from various research groups is carried out in order to reliably understand the complicated chemical kinetics defining the reactive species densities. Atomic oxygen densities in parallel plate radio frequency driven He/O₂ micro-scaled atmospheric pressure plasma jets have been measured in the literature by several research groups with different methods including: two-photon absorption laser induced fluorescence (TALIF) spectroscopy and optical emission spectroscopy-based methods. These measurement data with a variation of the absorbed power, the He gas flow rate and the O₂ mixture ratio are simulated in this paper with a plasma-chemical plug-flow model coupled with a two-term Boltzmann equation solver. The simulated atomic oxygen densities are generally in good agreement with the measured ones. Specifically, particularly good agreement is achieved between the simulations and most of the TALIF measurements over a range of operating conditions. The model prediction accuracy relative to a subset of the TALIF measurements is quantified by the percentage error between the measured and simulated atomic oxygen densities. An approximate normal distribution is observed in the histogram plot of the percentage error, and the mean is close to zero. The mean is shifted positively and negatively in the case of removing important atomic oxygen gain and loss channels, which implies the underestimation and overestimation of the simulation results relative to the measurement data, respectively. This indicates that proper incorporation of the dominant reaction channels in the

* Authors to whom any correspondence should be addressed.



Original Content from this work may be used under the terms of the [Creative Commons Attribution 4.0 licence](https://creativecommons.org/licenses/by/4.0/). Any further distribution of this work must maintain attribution to the author(s) and the title of the work, journal citation and DOI.

simulations plays a key role in the model prediction accuracy, as expected. The manual analysis of the quantitative influence of the dominant reaction channels on the model prediction accuracy demonstrated in this work provides a basis for further studies on improving plasma-chemical reaction schemes based on systematic comparisons with large experimental data sets.

Keywords: micro-scaled atmospheric pressure plasma jet, COST-Jet, plug-flow model, atomic oxygen density, validation, model prediction accuracy

1. Introduction

A large variety of studies have been conducted on atmospheric pressure plasma jets [1–6] for their application prospects in the fields such as surface processing (e.g. etching, deposition) and biomedicine (e.g. bacteria inactivation, wound healing) [2–4], as well as gas conversion (e.g. CO₂ dissociation, NH₃, NO synthesis) [7–12]. Correspondingly, diverse configurations of atmospheric pressure plasma jets were developed [1–3, 5], and a wide range of fundamental experimental and computational studies were carried out [4–6]. Atmospheric pressure plasma jets are well suited to efficiently convert molecular gases into diverse reactive species, which are considered to play a major role in related applications such as bacteria inactivation [1, 2] and polymer modification [3, 4]. It was reported that the produced reactive atomic oxygen species is of key importance for the treatment of cancer cells [13] and polymer etching [14–16]. Furthermore, it was predicted in our previous work [17] that atomic oxygen has a significant influence on the production and destruction of nitric oxide, which has been suggested to be important in wound healing applications [18]. Therefore, a detailed study of the atomic oxygen density produced by atmospheric pressure plasma jets is important to improve the performance of the corresponding applications.

Reactive species densities are affected by the complex plasma chemistry, which consists of diverse interactions between neutrals and charged particles. A fundamental understanding of these rich chemical kinetics is necessary for the development and optimization of reactive species production. Numerous detailed reaction sets have been established, such as the He/H₂O sets by Liu *et al* [19] and Schröter *et al* [20], the He/O₂ sets by Liu *et al* [21] and Turner [22], the He/Air sets by Murakami *et al* [23–25] and Sun *et al* [26], and the Ar/air set by Van Gaens *et al* [27–29]. The reliability of the established plasma-chemical models are generally assessed by the validation between the simulated and corresponding measured reactive species densities. For instance, the validations were conducted for the densities of atomic oxygen and hydroxyl radicals [20], helium metastable and reactive oxygen species [23], ozone [27], atomic oxygen and nitric oxide [29], atomic oxygen [30] as well as argon metastable, ozone and nitrogen oxide species [31].

Simulation results during validation studies are mainly compared with the measurement data from a single type of plasma source from the collaborating experimental colleagues, and sometimes compared with those from diverse types of plasma sources in the literature. In the case of comparison with the data from a single type of plasma source, the inconsistency between the input parameters of the simulations

and measurements is minimized by the close collaboration between the modellers and their experimental colleagues. In the case of comparison with the data from diverse types of plasma sources, a key challenge is the diversity of plasma sources available and the related difficulty of ensuring that the models used are well-suited to represent the experimental system. However, when such studies are carried out they have the advantage of a larger range of data to compare with models. The advantages of both comparison approaches can be obtained by comparing simulations with experimental data from similar types of plasma sources, where comprehensive measurement details are available and where the same quantity has been measured in each study. Ideally, such studies will also have been carried out in a number of publications from different research groups. In these validation cases, the aforementioned inconsistency, the influence of the model limitations and experimental errors can be mitigated. Consequently, the reliability of the established chemical model can be assessed and further improved by this kind of validation. However, such validation is still lacking in the literature to the knowledge of the authors.

The development and optimization of reactive species production is one of the main research goals of parallel plate radio frequency driven micro-scaled atmospheric pressure plasma jets (μ APPJs), which have the advantages of the miniature and simple design for an easy and safe operation and a localized treatment [32]. The atomic oxygen densities produced by μ APPJs has been of interest for a number of years, and multiple publications from various groups reported corresponding density measurements [15, 33–39]. These radio frequency driven μ APPJs [15, 33–39] work on a similar principle, i.e. the feed gas flow is perpendicular to the electric field generated between two parallel planar electrodes. Many of these μ APPJs are related to the COST-Jet, i.e. the European COST (Cooperation in Science and Technology) Reference Microplasma Jet [32]. Specifically, these μ APPJs are the COST-Jet [35–38], the COST-Jet prototypes [15, 33, 34], and a capillary jet device where the mechanical and electrical design and operating principle are similar to those of the COST-Jet [39]. More details of these μ APPJs are provided in section 2. It is worth to explicitly note that accurate measurements of the absorbed power in the plasma, one of the most important input parameters for simulations, can be provided by the recent experimental studies of μ APPJs [15, 35–39]. Therefore, the inconsistency between input parameters of the simulations and measurements can be reduced compared to earlier studies where the measurement of absorbed power was not regularly performed. Furthermore, the COST-Jet [35–38] was developed as a reference source in accordance with a

series of prototype sources used in the years before. The reproducibility of the COST-Jet was maximised by Golda *et al* [32] with a large amount of effort such as the refinement of the mechanical and electrical design. A comprehensive validation between the experiments and simulations should be enabled by the well-characterised nature of these jets and the substantial amount of effort that has been invested in the measurement of atomic oxygen densities in them.

The prediction accuracy of the simulated reactive species densities relative to the corresponding measurement data is one of the key issues for plasma modelling. Quantification of the prediction accuracy was reported by several publications [22, 40–42], i.e. the influence of the uncertainty of the simulation input parameters, especially a large number of reaction rate coefficients that are subject to error, on the simulation output results. It was indicated by Turner [22, 40] that the uncertainty of the rate coefficients in the He/O₂ chemical model results in the uncertainty of the calculated species densities. Such a density uncertainty is a factor of two to five in most cases, however it is even more than a factor of ten in some extreme cases [22]. It was presented by Berthelot *et al* [41] and Wang *et al* [42] that different combinations of rate coefficients based on their uncertainties are used to predict the uncertainty of the simulation output results such as uncertainty of electron density and temperature (15%) in the CO₂ plasma [41], uncertainty of CO₂ and CH₄ conversion (24% and 33%, respectively) [42]. Furthermore, the complex chemical model (almost 400 reactions) for the conditions relevant to biomedical applications was simplified (about 50 reactions), and in the sensitivity analysis around 10 reaction rate coefficients were found to cause most of the uncertainty [40]. The reaction rate coefficients primarily responsible for the uncertainty in the relevant model prediction are also identified in [41, 42]. Attention to these critical rate coefficients, i.e. resulting in the uncertainty, can contribute to a huge improvement in the model prediction accuracy.

Good prediction accuracy can be achieved by including the key reactions in the chemical model as comprehensively as possible. Recently, the Quantemol database developed by Tennyson *et al* [43] has been devoted to providing data on all the relevant chemical kinetics that could be important in the plasmas. For instance, a fast algorithm was developed by Hanicinec *et al* [44] to output the key reaction set defining the species density of interest, and a regression model was trained by the same group [45] on available reaction and species data extracted from the multiple databases to fast approximate the unknown rate coefficients of the involved chemical kinetics. The former focuses on filtering out the key reactions, while the latter provides the opportunity to find the potentially important reactions.

The prediction accuracy can be confirmed by the agreement between the simulation results and measurement data, as noted earlier [20, 23, 27, 29–31]. However, the presented agreement is typically validated by a qualitative assessment. Specifically, the simulation results and the measurement data under certain operating conditions are simultaneously shown in a figure, and an agreement is assessed qualitatively instead of with quantitative number. In other words, discussion of the

prediction accuracy in terms of quantification of the agreement between the simulated and measured species densities is relatively rarely carried out in the literature of plasma modelling. Such a quantification can be potentially obtained by a number of metrics. Recently, in other areas of computational chemistry, multiple metric approaches for the purpose of quantifying the prediction accuracy were reported by Vishwakarma *et al* [46]. These metrics can be used to quantitatively assess the quality, reliability and applicability of a given model, and to further compare the performance of the different models. For example, in the context of plasma modelling, the mean deviation between the simulation results and experimental datasets can be quantitatively assessed, and the influence of an absence of the key chemical reactions on the species density of interest can be quantitatively evaluated. This approach is most promising where large experimental datasets are available.

It should be emphasized that the prediction accuracy as a function of the deviation between the simulations and measurements is determined by diverse factors such as model limitation, experimental error, and potential inconsistency between the input parameters of the simulations and measurements. The influence of the model limitation on the prediction accuracy can be mitigated to some extent by attention to uncertainty of the critical rate coefficients [22, 40–42] and by a focus on filtering of the key reactions [43–45], as discussed above about the work of the shown publications. In the current work, the main aim is to systematically, and quantitatively compare the simulated atomic oxygen densities with a large range of experimental data from multiple publications of various research groups using similar plasma sources and different measurement methods.

The focuses of this study are summarized as the following two points:

- In section 5.1, the atomic oxygen density simulation results of this work are validated against the measurement data from multiple publications, which were conducted under different operating conditions, e.g. the absorbed power, the gas flow rate and the mixture ratio.
- In section 5.2, the agreement between model and experiment are critically assessed, and a subset of the available experimental data are selected in order to quantify the prediction accuracy of the simulated atomic oxygen densities through the percentage error between the simulation results and measurement data. The influence of removing the dominant atomic oxygen gain and loss reaction channels from the model on the prediction accuracy of the model is also quantitatively revealed.

The μ APPJs simulated in this paper are discussed in section 2. The pseudo one dimensional plug-flow model providing the one dimensional spatially resolved simulation results along the gas flow direction used in this study is described in section 3. The considered plasma-chemical reaction scheme is described in section 4. The key results are summarized in section 6.

2. Experimental model system

The μ APPJs [15, 33–39] are simulated in this study, i.e. the COST-Jet [35–38], the COST-Jet prototypes [15, 33, 34], and a subsequent evolution design of the COST-Jet [39]. Specifically, the atomic oxygen densities in the plasma channel and in the near effluent (at 1 mm distance from the plasma channel exit) of the aforementioned radio frequency driven He/O₂ μ APPJs [15, 33–39] measured with different methods in multiple publications by various groups are simulated with the theoretical approach and the chemical kinetics provided in sections 3 and 4, respectively. The rectangular plasma channels of these μ APPJs are designed as a cross-field configuration, i.e. the generated electric field between the two parallel planar electrodes is perpendicular to the feed gas flow. The feed gas is injected through one side of the two smallest cross sections, and exhausted from the other side. Good optical access for species density measurements is provided by the two side glass plates. For further details regarding the structures of these μ APPJs, see [15, 33–39]. The schematic structure of the COST-Jet [35–38] is shown in figure 1 as an example of these μ APPJs.

In section 5, several μ APPJs [15, 35–39] are considered. The μ APPJ by West [15], as a prototype, was investigated to inform the construction and operation of the COST-Jet [32]. The μ APPJs in the recent studies reported by Riedel *et al* [35], Myers *et al* [36] and Steuer *et al* [37, 38] are the COST-Jet. The μ APPJ provided by Winzer *et al* [39] is similar to the COST-Jet. However, they are slightly different, i.e. dielectric glasses were additionally assembled on the electrode surfaces confining the plasma in [39] to prevent a glow-to-arc transition at high absorbed power values so that the plasma is still stable at higher powers. The absorbed power value in the plasma is available in the experimental reports of the aforementioned μ APPJs [15, 35–39]. The absorbed power, which is important for the electron-impact processes in appendix A such as ionization and excitation mechanisms, is a key input to the pseudo one dimensional plug-flow model used in this work. Because it is directly available in the experimental studies, no further assumptions are required to use it in the model. It should be emphasized that the gas impurity and power uncertainty were reported as major reasons for the irreproducible experimental results of μ APPJs prior to the development of the COST-Jet [32]. A large amount of effort was conducted by Golda *et al* [32] for the COST-Jet to avoid the gas impurity (e.g. with the sealing improvement) and avoid the uncertainty of measured absorbed power (e.g. with integrated probes). Therefore, the potential errors as a result of the inconsistency between the input parameters of simulations and measurements are further minimized. This prompts a more precise comparison of the simulation results to the measurement data. The comparisons between our simulation results and the measurement data of the μ APPJs [15, 35–39] are shown and discussed in section 5. Note that the atomic oxygen densities produced by similar μ APPJs were also reported by other literature, e.g. the density measurement data in the effluent by Willems *et al* [47] and those in the plasma channel under a peak-to-peak voltage value of 500 V by Korolov *et al* [48]. However, such μ APPJs (e.g.

[47, 48]) are not simulated in this work attributing to our focus on the density in the plasma channel, and near effluent, and the necessity of knowing the absorbed power used in the simulations for this work.

In appendix B, the μ APPJs reported by Waskoenig *et al* [33] and Bibinov *et al* [34] are also simulated. These are prototypes of the COST-Jet [32]. In these studies, only the generator power and not the power absorbed in the plasma was reported. In our previous study [17] a power transfer efficiency of 5% between the generator input power and plasma absorbed power was assumed in order to simulate the measurement data. These two μ APPJs are simulated in this study with the same operating conditions reported in [17], but using the plug-flow model in section 3 and the updated and supplemented chemical kinetics in this work given in section 4 and appendix A. Note that the corresponding simulation results shown in B are only used as a comparison with those in our previous study [17], since the 5% power transfer efficiency (not used in section 5) used for the previous prototypes of the COST-Jet [33, 34] in appendix B and [17] is not a well-defined assumption and could lead to potential inconsistencies between the input parameters of measurements and simulations. In order to avoid these potential inconsistencies, these simulation results in appendix B are not analyzed in section 5.

Key information about the above-mentioned He/O₂ μ APPJs [15, 33–39] is summarized in table 1 including the measured atomic oxygen densities, the number of data points available, the plasma channel size, the He gas flow rate, the O₂ mixture ratio, the absorbed power in the plasma, the position of the atomic oxygen density measurements and the corresponding method used for the density measurements. It should be emphasized, that experiment and model are not always compared at exactly the same spatial location. This either because assumptions have had to be made about the exact spatial location of the measurement, or because measurements were carried out in the near effluent region, and the model used in this work is not adapted for the effluent. In both cases, the corresponding experimental measurements are compared with simulated densities at the nozzle of the plasma jet. The implications of these limitations are discussed later.

Precise plasma channel pressure values were not provided in [15, 35–39], therefore 1×10^5 Pa is used in our simulations for the μ APPJs shown in section 5. The gas temperatures used in the simulations of these μ APPJs are estimated from the experimentally measured relationships between the effluent gas temperature and absorbed power provided in [35, 39]. Note that [35] (P. 5) provided the relationship at $z = 3$ mm (i.e. in the effluent and 3 mm distance from the plasma channel exit) in an absorbed power range of 0.2–1.0 W, while [39] (P. 6-7) provided the relationship at $z = 0$ mm (i.e. at the plasma channel exit) in an absorbed power range of 0.5–6.0 W. The relationship of gas temperature versus absorbed power is roughly linear in both [35, 39]. The gas temperatures at $z = 3$ mm [35] are overall smaller than those at $z = 0$ mm [39] around 5–30 K in the absorbed power range of 0.06–6.50 W. Averaged values of the aforementioned gas temperature data between [35, 39] at the considered absorbed powers are estimated in this study

Table 1. Measured atomic oxygen densities, number of data points, operating conditions, measurement positions and methods (i.e. TALIF, SEA and OES) of the μ APPJs. The studies simulated in this work are: Waskoenig *et al* 2010 [33], Bibinov *et al* 2011 [34], West 2016 [15], Riedel *et al* 2020 [35], Myers *et al* 2021 [36], Steuer *et al* 2021 [37], Steuer *et al* 2022 [38], Winzer *et al* 2022 [39]. In section 5, in total, 118 TALIF measurement data points from 5 publications [15, 35–38] and 56 SEA measurement data points from 2 publications [38, 39] are used to compare with the simulation results of the current work, see section 2. A pressure of 1×10^5 Pa and gas temperatures as a function of absorbed power (see equation (1) in section 2) are used in the simulations for the μ APPJs [15, 35–39] shown in section 5. Following the values used in the simulations in our previous study [17], the experimentally defined gas temperatures of 345 K and 370 K and the chosen plasma channel pressures of 1×10^5 Pa and 101 325 Pa are used in our simulations for the μ APPJs in [33, 34], respectively, shown in appendix B.

reference: density range (10^{21} m^{-3}) & number of data points	Plasma channel size (mm^3)	He gas flow rate (sccm)	O ₂ mixture ratio (%)	Absorbed power (W) ^a	Measurement position (mm) ^b	Measurement method ^c
He/O₂ μAPPJs in section 5						
[15]: (4.41–17.25) & 15	$1 \times 1 \times 30$	1000	0.5	1.27–4.58	$z = 1^b$	ps-TALIF
[35]: (0.30–0.96) & 8	$1 \times 1 \times 30$	1000	0.5	0.20–1.00	$z = 1$	ps- & ns-TALIF
[36]: (1.00–4.39) & 4	$1 \times 1 \times 30$	1000	0.1–1.0	0.75	$z = 0^b$	ps-TALIF
[37]: (3.60–6.58) & 29	$1 \times 1 \times 30$	200	0.5	1.00	$z = -29 - 1$	ns-TALIF
[37]: (1.75–7.15) & 29	$1 \times 1 \times 30$	600	0.5	1.00	$z = -29 - 1$	ns-TALIF
[37]: (1.44–7.43) & 29	$1 \times 1 \times 30$	1000	0.5	1.00	$z = -29 - 1$	ns-TALIF
[38]: (1.19–3.72) & 4	$1 \times 1 \times 30$	1000	0.5	0.15–0.83 ^a	$z = -15$ or 0^b	ns-TALIF
[38]: (4.43–7.30) & 4	$1 \times 1 \times 30$	1000	0.5	0.08–0.73 ^a	$z = -15$ or 0^b	SEA
[39]: (5.96–37.00) & 12	$1 \times 1 \times 40$	1000	0.5	0.50–6.00	$z = -20$ or 0^b	SEA
[39]: (7.41–11.66) & 10	$1 \times 1 \times 40$	1000	0.2–2.0	1.00	$z = -20$ or 0^b	SEA
[39]: (19.20–24.54) & 10	$1 \times 1 \times 40$	1000	0.2–2.0	5.00	$z = -20$ or 0^b	SEA
[39]: (6.62–7.82) & 10	$1 \times 1 \times 40$	1000	0.5	1.00	$z = -38 - 5$	SEA
[39]: (10.20–20.03) & 10	$1 \times 1 \times 40$	1000	0.5	5.00	$z = -38 - 5$	SEA
He/O₂ μAPPJs in appendix B						
[33]: (2.21–4.35) & 13	$1 \times 1 \times 40$	995.0249	0.5	0.40–1.00	$z = -20$	ns-TALIF
[34]: (1.83–8.97) & 20	$1 \times 1.3 \times 40$	1500	1.5	1.5	$z = -38 - 0$	OES ^c

^a Applied driving voltage instead of absorbed power was given in [38]. Since both μ APPJs in [35, 38] are the COST-Jet and were operated with the same conditions, the reported absorbed power of [38] in table 1 is interpolated from the characteristics of absorbed power versus driving voltage measured in [35] (P. 5).

^b $z < 0$ mm, $z = 0$ mm and $z > 0$ mm represent the region of plasma channel, plasma channel exit and plasma effluent, respectively. The measured atomic oxygen densities as a function of the absorbed power [15] (P. 99) are considered in the current work, while the corresponding measurement position was not explicitly reported in [15] (P. 99). However, the atomic nitrogen and oxygen densities as a function of the applied voltage [15] (P. 98) were reported to be measured in the near effluent of the μ APPJ. Furthermore, the atomic nitrogen densities as a function of the N₂ mixture ratio [15] (P. 53) were reported to be measured at $z = 1$ mm. Therefore, we assume that the atomic oxygen densities as a function of the absorbed power [15] (P. 99) considered in the current work were also measured at $z = 1$ mm in [15] (P. 99). The measured atomic oxygen densities as a function of the mixture ratio [36] (P. 9) are considered in the current work, while the corresponding measurement position was explicitly reported at $z = 0$ –10 mm in [36] (P. 9) and thus the densities at $z = 0$ mm are considered. The measured atomic oxygen densities as a function of the absorbed power and the mixture ratio [38, 39] are considered in the current work, while the corresponding measurement position was not explicitly reported for certain data points in [38, 39]. For comparison with these data, simulations at $z = 0$ mm are used.

^c The measurement methods and errors are briefly summarized in section 2. The OES approach for the atomic oxygen density measurement was assisted by numerical simulation.

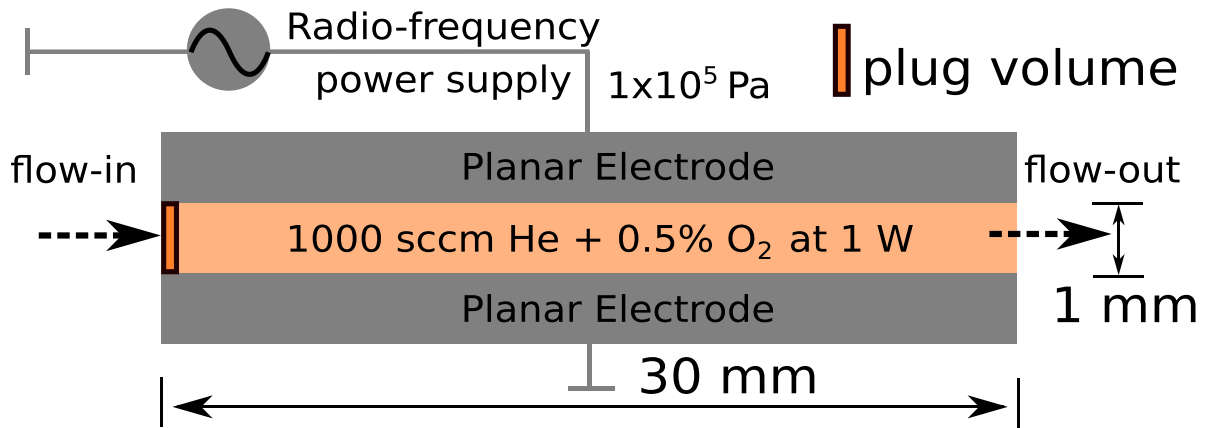


Figure 1. Schematic structure of the COST-Jet [35–38] shown as an example of the μ APPJs [15, 33–39] simulated in this work. The $1 \times 1 \times 30 \text{ mm}^3$ rectangular plasma channel of the COST-Jet [35–38], consists of two planar electrodes and two side glass plates. The jet used in [39] has slightly different dimensions, and also incorporates a glass capillary that also covers the electrodes, in contrast to the COST-Jet. Typical gas flows and plasma power are labelled. In the simulations, the plug volume moves in the direction of the gas flow based on its velocity. The figure is not scaled.

to be the following fit function:

$$T_g(\text{K}) = 302.6591 + 34.4318 P_{\text{abs}}(\text{W}), \quad (0.06\text{W} \leq P_{\text{abs}} \leq 6.50\text{W}), \quad (1)$$

where T_g in Kelvin is the gas temperature, and P_{abs} in Watt is the absorbed power in the plasma. These estimated temperature values are assumed to be a reasonable approximation of the volume-averaged gas temperatures in the plasma channel region for $z < 0 \text{ mm}$. In principle, the gas temperatures in each jet should scale with power density, as opposed to the total absorbed power. Since the structures and volumes of the plasma channels in [15, 36–38] are identical to those in [35], either power or power density can be used in the fit function for the gas temperature. On the other hand, the volume of the plasma channel in [39] is different from those in [15, 35–38], i.e. the same absorbed power corresponds to the different absorbed power density. However, a reasonable fit to all data is achieved using absorbed power as the scaling parameter, so this scaling is applied in section 5 in this work. In addition, it is observed in our simulations (not shown here) that the atomic oxygen densities as a function of power are similar for the simulations of the μ APPJ [15] for a varying gas temperature with equation (1) and those for a constant of 350 K. In other words, the atomic oxygen densities are not particularly sensitive to the gas temperature under the considered operating conditions. Furthermore, an approximately constant gas temperature for a varying O₂ mixture ratio was experimentally reported by the He/O₂ μ APPJ [39] (P. 6), so the gas temperature in the simulations is assumed not to change with varying O₂ mixture ratio.

The simulated atomic oxygen densities in this work are compared with the corresponding measured ones using different methods: including two-photon absorption laser induced fluorescence (TALIF) spectroscopy [15, 33, 35–38], helium

state enhanced actinometry (SEA) [38, 39] and optical emission spectroscopy (OES), assisted by numerical simulations [34]. In order to better understand the potential deviation between the simulation results and measurement data, it is of importance to be aware of the fundamental principles of the different measurement methods. Furthermore, due to the focus on simulations in this work, only a brief introduction to the three measurement methods mentioned above is given below.

In TALIF, the energy of two laser photons is used to excite a ground state atom of interest [15] (P. 29). The effective decay rate (i.e. the reciprocal of the lifetime) of the excited atomic species is mainly affected by two factors: radiative decay, and collisional quenching with other species. The fluorescence photon as a part of the radiative decay is emitted during the de-excitation of the atomic species, and subsequently a fluorescence signal is measured [15] (P. 34). Collisional quenching plays a more important role in the excited atomic species decay at higher pressures, and it is regarded as one of the largest possible sources of errors [15] (P. 32) during the evaluation of the aforementioned effective decay rate. The effective decay rate is one of the most important parameters affecting the evaluation of the ground state atom density of interest [15] (P. 35,37). The absolute density of the ground state atom is calibrated by using a noble gas, e.g. the xenon gas is used to calibrate the atomic oxygen density in the He/O₂ plasmas [15, 33, 35–38].

Picosecond (ps) laser systems have been used to directly measure the effective decay rate of the oxygen excited state in the ps-TALIF approach [15, 35, 36]. Such fast decay rates cannot be resolved by nanosecond (ns) laser pulses, and the effective lifetime is generally calculated on the basis of the gas mixture and known rate constants for collisional quenching in the ns-TALIF approach [33, 37, 38]. The accuracy of the effective lifetime calculation for the oxygen excited state in the effluent region is not guaranteed due to the uncertain quenching rate

coefficients and potentially unknown species concentrations [15] (P. 37), especially during mixing with ambient air [15, 35, 36]. In comparison, the calculation accuracy of the effective decay rate in the plasma channel region is in a reasonable degree as a result of the controlled feed gas [15] (P. 37), i.e. the dominant background gas He and defined O₂ admixtures [33, 37, 38]. Therefore, ps-TALIF has advantages for measurements in the effluent region [15, 35, 36], while ns-TALIF should be well-suited for those in the plasma channel region [33, 37, 38].

The atomic oxygen density measured with the SEA approach [38, 39] builds on the methods of classical actinometry and energy resolved actinometry [49, 50]. The density measured with the classical actinometry is determined from the intensity ratio of two spectral lines. One spectral line is from the gas to be studied (specifically from an excited oxygen state), and the other is from the actinometer gas of known density (typically from an excited argon state). Only direct electron-impact excitation is assumed in the classical actinometry approach to produce the oxygen and argon excited states from the respective ground states. The potentially important dissociative electron-impact excitation is neglected in the classical actinometry, but is considered in the energy resolved actinometry to improve the accuracy of the atomic oxygen density measurements [50] (P. 2). A third spectral line (from another excited oxygen state) is introduced in the energy resolved actinometry, and this allows for the simultaneous measurement of both the atomic oxygen density and the local mean electron energy [49] (P. 2). In the SEA approach, the aforementioned third spectral line in the energy resolved actinometry is replaced with the spectral line from an excited helium state. Several improvements are achieved in the SEA measurements compared to the energy resolved actinometry, e.g. the improved precision of the measured mean electron energy [38]. In the OES approach used in [34], the atomic oxygen density is determined from the spectral transition intensity, the cross-sections of the excitation processes, and the electron density as a function of the measured nitrogen molecular emission intensities and the simulated electron velocity distribution function. For further details of the TALIF, SEA and OES approaches, see [15, 33–39].

Experimental errors are inevitable, leading to uncertainties of the measured species densities. Because of this it is important to be aware of the error sources and the error values for reasonable comparison between the simulation results and measurement data. As a result of the focus on simulations in this work, only a general summary of the key information based on the experimental errors reported in the publications [15, 35–39] in table 1 is given in the following text.

The sources of the experimental errors can be due to diverse factors. West [15] (P. 52) collated the error sources of the TALIF measurements in a table, such as the systematic error (due to quantum efficiency, optical transmission, branching ratio, natural lifetime, two-photon excitation cross section ratio) and the stochastic error (due to normalised line profile, effective decay rate, laser energy, iCCD response). The two-photon excitation cross section ratio was noticeably shown as

the main source of error of around 50% [15] (P. 52). Similar error values [51] (P. 9369), [52] (P. 2335) and a lower value [53] (P. 382) were also reported in previous TALIF studies. The two-photon excitation cross section ratio was recently experimentally investigated for the TALIF measurement of atomic oxygen density [54] (P. 17), [55] (P. 16), and a definitive conclusion on the accuracy of the cross section ratio remains open [55] (P. 16). Steuer *et al* [38] and Winzer *et al* [39] stated that the error sources of the SEA measurements are from the uncertainty of the calculated values, such as the optical branching ratio and the effective excitation rate used to calculate the optical emission intensity ratio [39] (P. 7,8), [38] (P. 2,3), and also from the systematic uncertainty caused by the numerous assumptions of actinometry [38] (P. 5).

The values of the experimental errors were accordingly reported in the publications [15, 35–39]. However, the situations differ among these reports. A systematic error of 25% and a stochastic error of 14% were reported by West [15] (P. 98) in a figure caption of the measured atomic oxygen density as a function of the applied voltage, while the error values for the density as a function of the absorbed power were not explicitly given [15] (P. 99). Only the measured density as a function of the absorbed power [15] (P. 99) is compared with the current modelling study due to the necessity of the absorbed power used in the simulations. The error values around <15% were directly depicted by Riedel *et al* [35] (P. 8) in the figure of the measured atomic oxygen density as a function of the absorbed power, while the error margins of the density were estimated from the error margins of the absorbed power. Additional systematic error of more than 20% due to the uncertainty of the two-photon excitation cross section ratio was not included in the aforementioned depicted error values, since it does not affect the focus, i.e. the relative comparison of the investigated four COST-Jets [35] (P. 8). An error value of 36.9% for the measured atomic oxygen density was concluded by Myers *et al* [36] (P. 5) in a table together with diverse error sources such as the two-photon excitation cross section ratio. The error values of better than 50%–60% for the measured atomic oxygen density were stated by Steuer *et al* [37] (P. 4) due to the uncertainties of the constants used in the calibration procedure, but the deviation of the reproducibility for the relative trends is less than 20% taking advantage of the stable experimental system [37] (P. 4). The error values of the TALIF measurements by Steuer *et al* [38], explicitly plotted in the figure of [38] (P. 5), follow the values of Steuer *et al* [37] (P. 4), i.e. better than 50%–60% for the considered discharge conditions. These values [37, 38] are based on the data reproducibility and the noble gas calibration with xenon [38] (P. 4), which were provided with more details in [48]. The influence of the choice of the two-photon excitation cross section ratio [54] on the aforementioned error values was not incorporated [38] (P. 4). The error values around <15% of the SEA measurements by Steuer *et al* [38] were explicitly plotted in the figure of [38] (P. 5), while these values indicate only the uncertainty of the calculated values, and do not indicate the systematic uncertainty caused by the numerous assumptions of actinometry [38] (P. 5). The error values around <15% of the

SEA measurements by Winzer *et al* [39] were explicitly plotted in the figures of [39] (P. 8), while these values also indicate only the uncertainty of the calculated values [39] (P. 7).

Overall, in section 5, the measured atomic oxygen densities in 6 publications [15, 35–39] are used to compare with the simulation results of the current work. In total, 174 data points are considered in the current work: 118 TALIF measurement data points from 5 publications [15, 35–38] and 56 SEA measurement data points from 2 publications [38, 39]. A breakdown of the number of points considered from each publication is given in table 1. The experimental errors of these measured atomic oxygen densities can be stated to be mostly within the range of $\pm 50\%$ according to the summary of the reported error values mentioned above, although the situations differ among the error reports in [15, 35–39]. Therefore, the deviations between the measured and simulated atomic oxygen densities are inevitable due to the reported experimental errors for an upper limit of $\pm 50\%$. Furthermore, these deviations can be due to not only the reported experimental errors but also the potential model limitations and the potential inconsistencies between the input parameters of the measurements and simulations. Because of these factors, it should be emphasized that it is reasonable and realistic to pursue close rather than perfect agreement between the simulation results and each set of measurement data considered in the current work, since both have uncertainties.

3. Model

Pseudo one dimensional plug-flow models have been reported in a number of publications [17, 20, 25, 27–29, 56]. A pseudo one dimensional plug-flow model identical to that in our previous study [17] is used in this work. The only exception is that the wall loss of ions is not considered in this study, since at atmospheric pressure the simulation results including these losses do not significantly change relative to those excluding them [57] (P. 5). For instance, such a maximal change is only around 5% for the atomic oxygen density and other reactive oxygen species densities, as well as the dominant positive and negative ion densities simulated at the plasma channel exit of the COST-Jet under a typical operating condition in table 3. Maximal changes of around 5%, 5%, 20% and 10% are obtained in the test simulations for other plasma channel size, gas flow rate, mixture ratio and absorbed power in table 1, respectively.

The details of the model used in this work were given in [17], so only a brief summary is provided as below. The model solves the species particle balance equations and an electron energy balance equation to obtain the time resolved plasma properties including species concentrations and effective electron temperature in an infinitesimal plug volume, see figure 1. It should be emphasized that this plug volume comoves with the gas flow, therefore the time evolution of the plasma properties in this volume obtained from the balance equations is mapped to the one dimensional spatial position in the gas flow direction according to the gas flow velocity, see equation (5) in [17]. The aforementioned effective electron

temperature is corresponding to the mean electron energy of a non-Maxwellian electron energy distribution function (EEDF) [58, 59]. The non-Maxwellian EEDF is self-consistently calculated by calling a Boltzmann solver, i.e. the open-source simulation tool Lisbon kinetics Boltzmann (LoKI-B) published by Tejero-del-Caz *et al* [60]. This tool solves a time and space independent form of the electron Boltzmann equation under the two-term approximation, for non-magnetized non-equilibrium low-temperature plasmas excited by direct current (DC) or high frequency (HF) electric fields [60] (P. 1). The DC and HF models have different ranges of validity based on the electron collision frequency and the oscillation frequency of the applied field. Using the typical pressure, gas temperatures and gas mixture used under our conditions, and the validity criterion given in [60] (P. 10) for the high HF model, it is found that the HF model is strictly valid for driving frequencies much greater than 30 MHz. The jets studied in this work operate at a driving frequency of 13.56 MHz. Since these frequencies are in the same range, both the HF and DC models have been tested for our conditions. Both are found to yield almost identical EEDFs, and while it is not strictly valid under our conditions, the HF model has been applied for the simulations carried out in this work. Note that the electron kinetics are mainly controlled by the background helium and oxygen densities, since they are dominant and virtually invariant under the considered operating conditions in this study. For the sake of reducing the simulation duration, the EEDFs obtained from the Boltzmann solver for a corresponding steady-state plasma composition is used during the whole time evolution of the plasma properties in the plug-flow model. For further details of the aforementioned self-consistent calculation of the EEDF, see [17]. The plasma channel gas temperature used in the simulations is estimated from the experimentally defined relationship between the effluent gas temperature and absorbed power provided in [35, 39], see section 2. For further details of implementing the plug-flow model, see [17].

One focus of this work is dedicated to establishing an accurate He/O₂ chemical kinetics (see section 4) through the systematic validation between the simulated and measured atomic oxygen densities from a number of publications [15, 35–39]. An important consideration while doing this is to ensure that measurement and simulation are compared at suitable spatial locations within the jet. The plug-flow model in this work is limited to only properly calculate the plasma properties in the plasma channel region, while a model for the effluent region is not implemented here. This places some limitations on our ability to compare with measurements taken just outside of the jet channel. Overall, the measurement data were collected from different positions in the jet channel or near effluent, as described in table 1. With respect to comparing with measurements in the effluent, it was experimentally confirmed by Willems *et al* [47] (P. 4) and Myers *et al* [36] (P. 9) under similar operating conditions as in [15, 35] that the atomic oxygen density in the effluent region of the μ APPJs monotonically decreases, and the deviations of the measured densities at $z = 1$ mm relative to those at $z = 0$ mm are less than 10%. In addition, the experimental data of [37] demonstrates that the

atomic oxygen density in the plasma channel region monotonically increases along the gas flow direction, and that densities in the middle of the plasma channel are relatively close to those at the exit of the plasma channel. The density deviations between the two positions are less than 15%.

In other words, the atomic oxygen densities at the plasma channel exit are comparable with those at the middle of the plasma channel region and those in the near effluent region ($z = 1$ mm) for the operating conditions of the measurements considered in the current work. Therefore, for the sake of consistency in section 5, only the plug-flow model calculation results at the plasma channel exit are used to compare with the measurement data that were collected at the exit of the plasma channel region [36], in the near effluent region ($z = 1$ mm) [15, 35], and for cases where the measurement location was not explicitly reported [38, 39]. The plug-flow model calculation results along the gas flow direction in the plasma channel region are used to compare with the corresponding one dimensional spatially resolved measurement data [37, 39].

4. Chemical kinetics

The species considered in the He/O₂ plasma are listed in table 2. All the reactions included in this work are reported in appendix A. The He/O₂ chemical model has been developed in our previous study [17]. Except the vibrational kinetics, the chemical model is mainly based on the reaction set for a study of the atomic oxygen density in a parallel plate radio frequency driven He/O₂ μ APPJ (i.e. the COST-Jet prototype) by Waskoenig *et al* [33]. Our simulation results of radio-frequency plasmas in [17] were benchmarked against the calculated electron density and electron temperature in [33]. These simulation results were also validated against the measured atomic oxygen densities in [33, 34], as well as the measured electron density and ozone density in [34]. In the current study, besides from the aforementioned two references, more measurement data of atomic oxygen density from a range of publications [15, 35–39] are compared with our simulation results in order to further validate and optimize the developed He/O₂ chemical model. For further details, see sections 2 and 5. It was predicted in [17] that the simulated atomic oxygen densities of the considered μ APPJs are not affected by the vibrationally excited oxygen molecules included in the chemical model. Therefore, for the sake of reducing the simulation duration, these vibrationally excited states are not considered in the chemical kinetics of this study.

To further optimize the He/O₂ model, numerous updates and supplements are conducted in this study based on the chemical kinetics developed in our previous work [17]. All the updates and supplements are remarked in appendix A. For the sake of simplicity, only several key points are summarized as follows:

- (1) The electron-impact reactions in tables A1–A5 are incorporated in the 0-D model and LoKI-B solver according to the IST-Lisbon database, which yields good agreement between calculated and measured swarm parameters with the helium complete set [61, 62] and also yields good agreement with oxygen complete set for E/N values between 10 and 1000 Td [62, 63]. Only the cross-section data belonging to the complete set [61–63] are used in the solution to the Boltzmann equation [60] for cases marked with $f(\epsilon)$ in the aforementioned tables, while those (not part of the complete set [61–63]) are directly evaluated to calculate rate coefficients according to the calculated EEDF for cases marked with $f(\sigma)$ in these tables. The energy loss as a result of the excitation from ground state to vibrationally excited states and higher electronically excited states shown in table A4 is considered since these excitation reactions are part of the complete set [61–63]. However, these vibrationally excited states and higher electronically excited states are not included in our He/O₂ model due to the lack of corresponding chemical kinetics data. In other words, the production and destruction reaction channels of these excited states are not considered, and therefore the corresponding state densities are not calculated.
- (2) The updates and supplements of the chemical kinetics in this work are based on a reaction mechanism for oxygen plasmas recently reported by Dias *et al* [64], since it was shown that their 0-D simulation results are in good agreement with the measured O(³P), O₂ electronically ground state, O₂(a¹ Δ_g) and O₂(b¹ Σ_{g^+}) densities in a DC glow discharge at low pressure. In order to better capture the production and destruction of O(³P), O₂(a¹ Δ_g) and O₂(b¹ Σ_{g^+}), an effort of updating and supplementing the corresponding reaction channels was conducted in [64]. In view of this, O₂(b¹ Σ_{g^+}) is additionally considered in our He/O₂ model shown in table 2. Furthermore, the rate coefficients in our previous He/O₂ model [17] are updated to those in [64] for cases of the same reaction channels present in [17, 64] shown in table A2, and the reactions absent in [17] but present in [64] are supplemented into this study shown in table A3. It is worth to note that the rate coefficients for three-body reactions are pressure dependent and may not necessarily be directly adapted from a reaction scheme developed at low pressure to one used at much higher pressures. In this case, we have mainly focused on the use of two-body rate coefficients from the study of Dias *et al* [64] and verified that the relevant three-body processes included in the reaction scheme are suitable for the pressures considered in this work.
- (3) The probabilities of the neutral wall reactions in table A6 are updated and supplemented in accordance with those in [64] (P. 8). Based on this the atomic oxygen wall recombination O(³P) + wall \rightarrow 1/2O₂ is included in this study with a probability of 0.002. This constant is estimated from the most frequent value of the probabilities as a function of pressure (30 – 1333 Pa) and discharge current (10 – 40 mA) for wall temperature (323 K) and wall material (Pyrex) reported in [64] (P. 8), which is based on a recent experimental study by Booth *et al* [65]. This constant is also close to the probability at the maximum pressure considered in [64] (i.e. 1333 Pa). This is a much lower pressure than the μ APPJs involved in the current

Table 2. The considered species in the He/O₂ model.

He/O ₂ plasma: He, He(2 ³ S), He ₂ [*] , He ⁺ , He ₂ ⁺ ,
O(³ P), O ₂ (X, v = 0), O ₃ , O(¹ D), O ₂ (a ¹ Δ _g), O ⁺ , O ₂ ⁺ , O ₄ ⁺ , O ⁻ , O ₂ ⁻ , O ₃ ⁻ , O ₄ ⁻ ,
<i>e</i>

Additionally considered species compared to our previous work [17]: O ₂ (b ¹ Σ _g ⁺)

work, so further discussion around the value of this probability is warranted.

The probability values of the atomic oxygen wall recombination reported in multiple publications for various pressures, wall temperature and wall materials (e.g. the stainless steel, quartz and Pyrex [66] (P. 29–32, 37) relevant to the μAPPJs involved in the current work) were recently collected in a review study by Paul *et al* [66]. The majority of these measurements are carried out at much lower pressures than those relevant for μAPPJs, so we can only take general insights from these. In general, it was shown in [66] (P. 41) that the recombination probability for atomic oxygen on glass surfaces is not strongly influenced by pressure in the range between 10 and 10 000 Pa. The probability values from multiple publications tend to show a large scatter between 10⁻² and 10⁻⁶. On metallic, and other semi-catalytic surfaces, the values of the atomic oxygen recombination probability are shown to generally decrease with pressure, with values above 100 Pa showing scatter in the range of 10⁻¹ and 10⁻³ [66] (P. 40). The value of 0.002 chosen in this work sits within the upper part of the range for glass surfaces, and the lower part of the range for metallic and semi-catalytic surfaces, and in this context seems a reasonable approximation for the surface materials of the μAPPJs studied.

The wall loss rate of atomic oxygen is implemented in the model using the formula for diffusion calculations in various simple geometries (e.g. the rectangular channel considered in the current work and the cylindrical channel used in [64, 65]) proposed by Chantry [67]. The transport of a neutral from the volume to the wall of the plasma channel calculated in the current work is explicitly given by equation (8) in [17] (P. 5). The equation as a function of the neutral wall reaction probability was discussed in detail in [67] (P. 1143–1144) and [59] (P. 314). The equation was also used in other publications such as [68] (P. 613), [69] (P. 405), [70] (P. 20) and [64] (P. 3).

It was reported in [64] (P. 12) and our previous study [17] (P. 10) that the probability of the atomic oxygen wall recombination used in the simulation results plays an important role in accurate prediction of the referenced measurement data. In other words, the atomic oxygen density is significantly affected by this wall recombination for the studied setup conditions reported in [17, 64]. The sensitivity of the simulated atomic oxygen densities to the probability of the atomic oxygen wall recombination is tested in figure B1(a). As the probability value is modified from 0 to 1, the variation of the atomic oxygen density is about a factor of 2 in the considered power range.

About 90% of this modification takes place at the probability value modified from 1 × 10⁻⁴ to 5 × 10⁻². The reference value of 0.002 used in this work locates in this sensitive range. Based on the discussion of the relevant data from the review of Paul *et al* [66], any uncertainty in the value of the recombination probability (i.e. 10⁻¹ and 10⁻⁶) also overlaps with this range. From this, we can conclude that uncertainties in the wall recombination probability of atomic oxygen are likely to be a significant part of the overall sensitivity in our simulation results. However, based on a lack of specific information on these probabilities for our conditions, it is not possible to quantify these beyond this general discussion.

It may be possible to reduce the uncertainty in the wall recombination probabilities in future work using a more comprehensive surface model. For instance, surface kinetics models such as that developed by Viegas *et al* [71] allow for surface recombination probabilities to be calculated based on rates of adsorption, desorption and reactions of adsorbed species. As such, these models allow for recombination probabilities to be calculated for specific plasma and surface conditions.

- (4) The partial supplements of the chemical kinetics shown in table A3 are conducted according to a simulation study of He/O₂-containing plasma recently reported by Brisset *et al* [72]. Their He/O₂ model was based on the work of Turner [22], which made an effort to quantify the uncertainty of the predicted species densities due to the uncertainty of the reaction rate coefficients. We conduct the corresponding supplements in this work, e.g. the reactions regarding more interactions between helium and oxygen species.

5. Results

5.1. Comparison between the simulated and measured atomic oxygen density

The O(³P) densities of the He/O₂ μAPPJs in a range of the absorbed power from around 0.06 W to 5.00 W measured by West 2016 [15], Riedel *et al* 2020 [35] and Steuer *et al* 2022 [38] together with the corresponding plug-flow model calculations of this work are shown in figure 2. It is found both by the measurements and simulations of the studied μAPPJs that the O(³P) densities increase monotonically with the increasing absorbed power. An agreement between the ps-TALIF measurement data of the COST-Jet prototype by West [15] and our simulation results in the absorbed power range of 1.00–5.00 W is obtained in figure 2(a). The measurement data

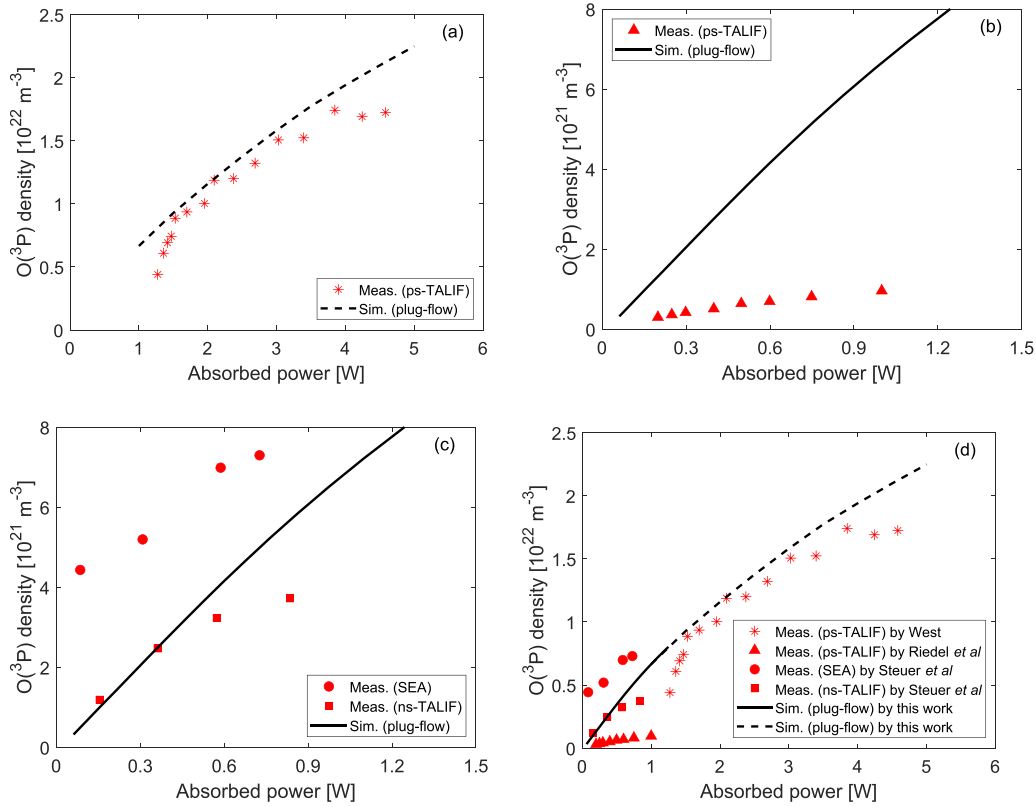


Figure 2. The $O(^3P)$ densities of the He/O₂ μ APPJs for a variation of the absorbed power from 0.06 W to 5.00 W. (a) The ps-TALIF measurement data in the near effluent at 1 mm distance from the plasma channel exit of the COST-Jet prototype reported by West 2016 [15] (*) and the plug-flow model calculations of this work (---). (b) The ps- & ns-TALIF measurement data in the near effluent at 1 mm distance from the plasma channel exit of the COST-Jet reported by Riedel *et al* 2020 [35] (\blacktriangle) and the plug-flow model calculations of this work (—). (c) The ns-TALIF (\blacksquare) and SEA (\bullet) measurement data in the plasma channel of the COST-Jet reported by Steuer *et al* 2022 [38] and the plug-flow model calculations of this work (—). The measurement data and model calculations provided in figures (a)–(c) are summarized in figure (d) for the sake of a straightforward comparison. The shown plug-flow model calculations are the simulation results at the plasma channel exit, see section 3. 1000 sccm He gas flow mixed with 0.5% O₂ are fed to the $1 \times 1 \times 30$ mm³ plasma channel of the aforementioned μ APPJs.

are slightly smaller than the simulation results. Part of the reason for this may be that the measurements were conducted in the near effluent at 1 mm distance from the plasma channel exit, while the simulations provide the values at the plasma channel exit. It was also reported by similar μ APPJs of Willems *et al* [47] and Myers *et al* [36] that the measured $O(^3P)$ densities in the near effluent at 1 mm distance from the plasma channel exit are slightly smaller than those at the plasma channel exit. Specifically, the deviations between the densities at both positions are typically in the range of 10%, see section 3. However, our simulation results at the plasma channel exit overestimate the ps- & ns-TALIF measurement data in the near effluent at 1 mm distance from the plasma channel exit of the COST-Jet reported by Riedel *et al* [35]. The overestimation is around a factor of 4.4–6.9 in the absorbed power range of 0.20–1.00 W presented in figure 2(b). Such a non-negligible overestimation may, for example, be partly due to the different simulation and measurement positions. Furthermore, there is also a degree of variation between the experimental measurements of Riedel *et al* [35], West [15] and Myers *et al* [36] in the near effluent, for similar plasma

operating conditions, with those of Riedel *et al* [35] tending to be lower. The reasons for these differences are unclear, but they serve to illustrate that there is a degree of variation in the densities reported in different publications. The ns-TALIF and SEA measurements were conducted by Steuer *et al* [38] in the plasma channel region of the COST-Jet. As discussed in more detail in table 1 and section 3, these measurements are compared to plug flow simulations at the exit of the jet. The ns-TALIF measurement data are well captured by our simulation results at the plasma channel exit as shown in figure 2(c). Our simulated mean electron energy (around 3 eV) is relatively close to the SEA measurement data (around 4.2 eV) in the absorbed power range of 0.08–0.72 W (not shown here). However, our simulated $O(^3P)$ density underestimate the SEA measurement data. The similar underestimation is also predicted in the simulations of figure 5, which also uses the SEA method. For a straightforward comparison, the measurement data and model calculations provided in figures 2(a)–(c) are summarized in figure 2(d). The overall trend and absolute values of the measurement data are captured by our model calculations.

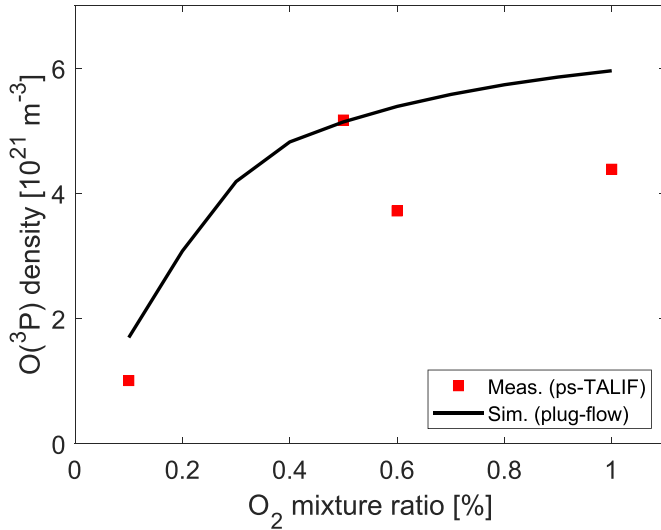


Figure 3. The $O(^3P)$ density of the He/O_2 μ APPJ for a variation of the O_2 mixture ratio from 0.1% to 1.0%. The density at the plasma channel exit of the COST-Jet was measured with the ps-TALIF approach by Myers *et al* 2021 [36] (■) and is simulated with the plug-flow model of this work (—). 1000 sccm He gas flow mixed with the depicted O_2 ratio are fed to the $1 \times 1 \times 30$ mm³ plasma channel driven by 0.75 W absorbed power.

The $O(^3P)$ density at the plasma channel exit of the He/O_2 μ APPJ (i.e. the COST-Jet) in a range of the O_2 mixture ratio from 0.1% to 1.0% measured by the ps-TALIF approach of Myers *et al* 2021 [36] together with the corresponding plug-flow model calculations of this work are shown in figure 3. It is observed both by the measurements and simulations under the considered operating conditions that the $O(^3P)$ density increases with increasing O_2 mixture ratio, and starts to saturate at 1.0% O_2 . Furthermore, similar measured and simulated $O(^3P)$ densities are obtained.

The one dimensional spatially resolved $O(^3P)$ density along the gas flow direction in the plasma channel region of the He/O_2 μ APPJ (i.e. the COST-Jet) for cases of feeding 200 sccm, 600 sccm and 1000 sccm He gas flow rate measured with the ns-TALIF approach by Steuer *et al* 2021 [37] together with the corresponding plug-flow model calculations of this work are shown in figure 4. Note that the measurement data, representing the $O(^3P)$ density along the gas flow direction at the middle between two electrodes, are obtained by averaging the measurement data at $x = 0.4$ mm and $x = 0.6$ mm of figure 2 in [37], which were provided in [73]. A good agreement between these measurement data and our model calculations is observed for a varying He gas flow rate. It is shown both by the measurements and simulations that for the lowest gas flow rate the $O(^3P)$ density is saturated at earlier locations in the plasma channel, while for a higher gas flow rate the $O(^3P)$ density is saturated only close to the plasma channel exit. This is due to the smaller residence time of the species in the plasma channel at a higher gas flow rate. It is shown by the simulation results of 1200 sccm He gas flow rate that the $O(^3P)$ density at the plasma channel exit is reduced by a further increasing gas flow.

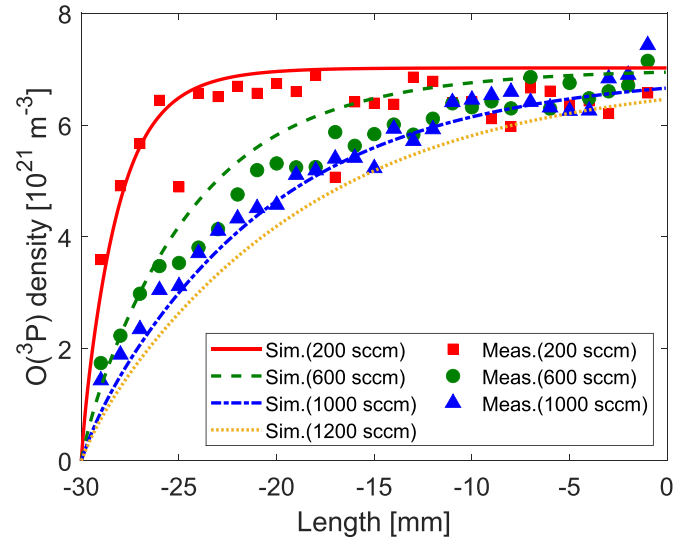


Figure 4. The one dimensional spatially resolved $O(^3P)$ density along the gas flow direction in the plasma channel region of the He/O_2 μ APPJ for a variation of the feed 200 sccm, 600 sccm, 1000 sccm, and 1200 sccm He gas. The solid points (200 sccm ■, 600 sccm ●, and 1000 sccm ▲) were measured with the ns-TALIF approach by Steuer *et al* 2021 [37]. The lines (200 sccm —, 600 sccm - - -, 1000 sccm - · - ·, and 1200 sccm · · · ·) are simulated with the plug-flow model of this work. The depicted He gas flow mixed with 0.5% O_2 are fed to the $1 \times 1 \times 30$ mm³ COST-Jet plasma channel driven by 1.00 W absorbed power.

The $O(^3P)$ densities of a He/O_2 μ APPJ (similar to the COST-Jet, but with a dielectric capillary between the electrodes) measured with the SEA approach by Winzer *et al* 2022 [39] together with the corresponding plug-flow model calculations of this work are shown in figure 5. As discussed in more detail in table 1 and section 3, the measurement data in figures 5(a) and (b) are compared to plug flow simulations at the exit of the jet. The simulated $O(^3P)$ densities as a function of the absorbed power, O_2 mixture ratio and plasma channel position in figure 5 underestimate the corresponding SEA measurement data. The similar underestimation is also observed in figure 2(c). However, our simulation results still capture the overall trend and quantity of the measurement data. In figure 5(a), the simulated and measured $O(^3P)$ densities increase with increasing absorbed power, and this is similarly predicted in figure 2. The larger deviation between the measurements and simulations at larger absorbed power may be ascribed to experimental variations, since for instance the simulated $O(^3P)$ density at 5 W in figure 5(a) (around 1.8×10^{22} m⁻³) agrees better with the measurement data under the same operating conditions in figures 5(b) (around 2.3×10^{22} m⁻³) and (c) (around 2.0×10^{22} m⁻³) compared to those in figure 5(a) (around 3.5×10^{22} m⁻³). It is indicated in figure 5(b) that both the measured and simulated $O(^3P)$ densities at 1 W and 5 W increase with increasing O_2 mixture ratio, and start to saturate at 1.0% O_2 (similarly observed in figure 3). In figure 5(c), the measured and simulated $O(^3P)$ densities at 1 W and 5 W increase continuously along the gas flow direction, and start to saturate at the middle of the plasma channel.

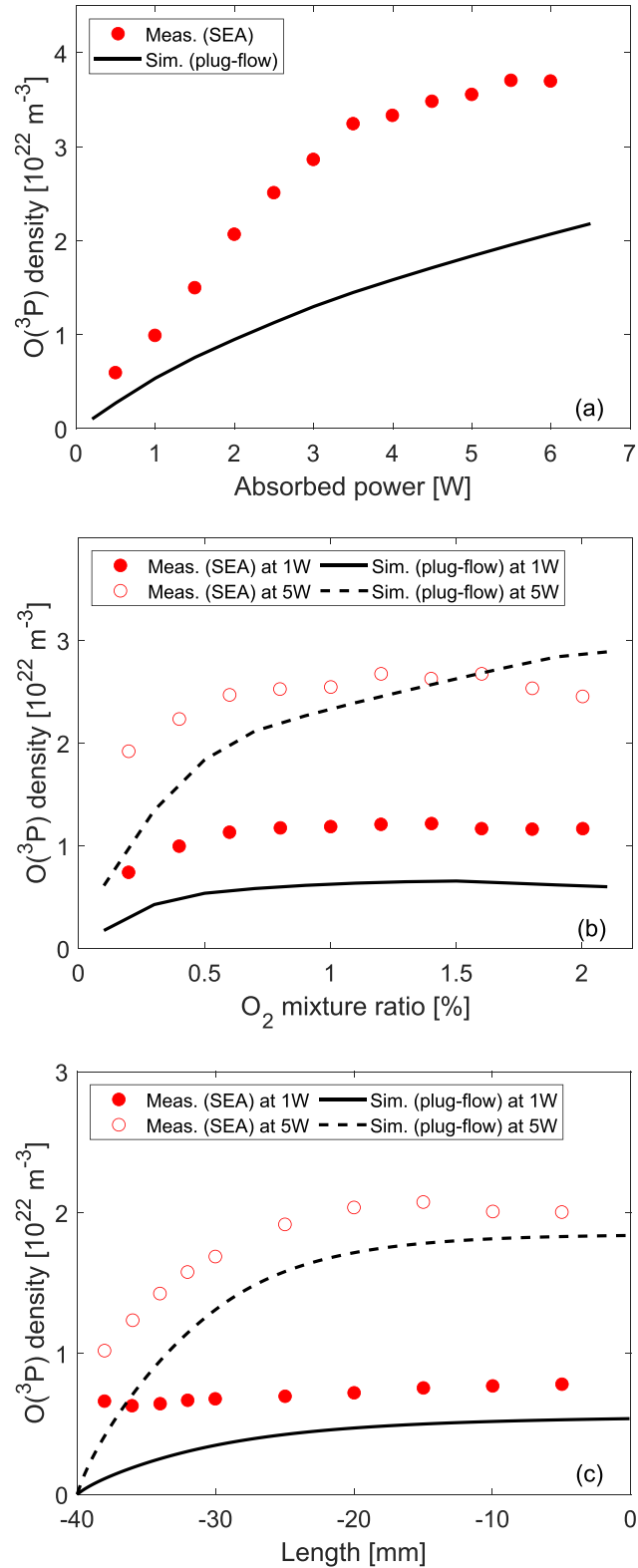


Figure 5. The $O(^3P)$ densities of the He/ O_2 μ APPJ reported by Winzer *et al* 2022 [39]. (a) The SEA measurement data in the plasma channel for a variation of the absorbed power from 0.5 W to 6.5 W (\bullet) and the plug-flow model calculations of this work (—). (b) The SEA measurement data in the plasma channel for a variation of the O_2 mixture ratio from 0.1% to 2.0% (\bullet and \circ at 1 W and 5 W absorbed power, respectively) and the plug-flow model calculations of this work (— and - - -). The plug-flow model calculation values shown in figures (a) and (b) are the simulation results at the plasma channel exit, see section 3. (c) The one dimensional spatially resolved SEA measurement data along the gas flow direction in the plasma channel region (\bullet and \circ at 1 W and 5 W absorbed power, respectively) and the corresponding plug-flow model calculations of this work (— and - - -). 1000 sccm He gas flow mixed with 0.5% O_2 (if not stated otherwise) are fed to the $1 \times 1 \times 40 \text{ mm}^3$ plasma channel.

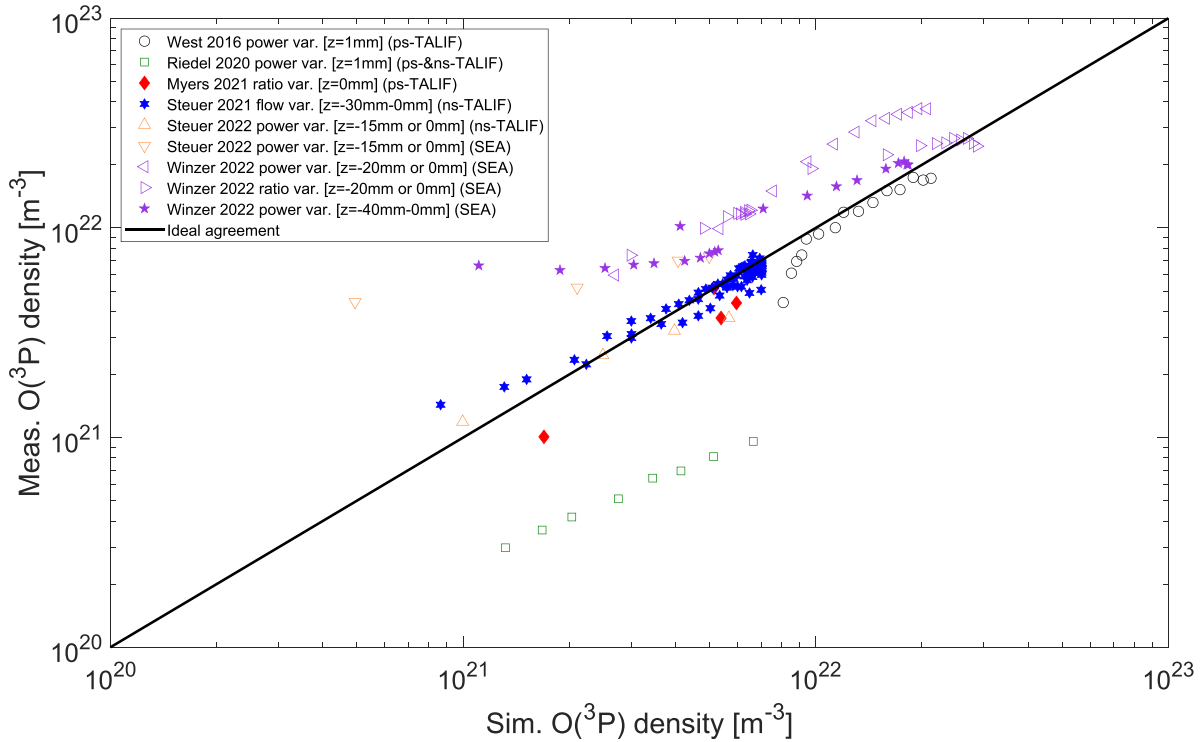


Figure 6. The measured atomic oxygen densities of several μ APPJs from multiple publications [15, 35–39] using the TALIF and the SEA measurement methods versus the corresponding simulated ones of this work using the plug-flow model. These density values are a summary of the validation data in section 5.1. The measurement data as a function of the absorbed power (‘power var.’), the He gas flow rate (‘flow var.’) and the O₂ mixture ratio (‘ratio var.’) were reported by West 2016 [15], Riedel *et al* 2020 [35], Myers *et al* 2021 [36], Steuer *et al* 2021 [37], Steuer *et al* 2022 [38] and Winzer *et al* 2022 [39]. The measurement data were collected at different positions in the jet. Further details on this, and the spatial locations in the plug-flow model that have been used to compare with the different experimental measurements are given in table 1 and section 3. Empty symbols are used to denote points for which measurement and model are not compared for exactly the same spatial location. While the discrepancies due to these limitations are expected to be comparatively small, these are pointed out to emphasize that comparisons with these measurements are expected to be less reliable than those denoted by filled symbols. The operating conditions of the measurements are the same as those of the corresponding simulations. Therefore, an ideal agreement between the measurement data and simulation results is illustrated by the black solid line, where the measured densities are equal to the simulated densities under the same operating conditions. In total, 174 data points are included, 118 TALIF measurements from 5 publications [15, 35–38] and 56 SEA measurements from 2 publications [38, 39].

5.2. Prediction accuracy of the simulated atomic oxygen densities relative to the measured ones

A summary of the validation data of the multiple μ APPJs in section 5.1 is presented with the measured atomic oxygen densities [15, 35–39] versus the corresponding simulated ones of this work in figure 6. Presenting the comparison between simulation and experiment in this way, the simulation results can be used as a common reference between the different experimental studies. From this, information on both the agreement between simulation and experiment can be obtained, as well as an assessment of the level of consistency between the different experimental data sets. In principle, an ideal agreement between the measured and simulated atomic oxygen densities is illustrated by the black solid line shown in figure 6, where the measured densities are equal to the simulated densities under the same operating conditions. However, a small deviation between the measured and simulated atomic oxygen densities is realistically inevitable, e.g. the slight influence due to model limitation, experimental error, and potential inconsistency between the input

parameters of the simulations and measurements. Therefore, points near the aforementioned black solid line can also be regarded as representing good agreement. Most values of the measurement data and simulation results in figure 6 are near the black solid line, and relatively evenly distributed on both sides. Specifically, a good agreement is observed between the simulations and most of the TALIF measurements with a variation of the absorbed power, the He gas flow rate and the O₂ mixture ratio. The simulation results are overall smaller than the SEA measurement data.

One focus of this work is dedicated to quantifying the prediction accuracy of our simulated atomic oxygen densities relative to the measured ones (see section 2), and further analyzing the influence of the absence of the dominant atomic oxygen gain and loss reaction channels on the aforementioned prediction accuracy. The prediction accuracy, as a function of the deviation between the measurement data and simulation results, is essentially influenced by factors such as model limitation, experimental error, and potential inconsistency between the input parameters of the simulations and measurements. It is visibly observed in figure 6 that the simulation results are

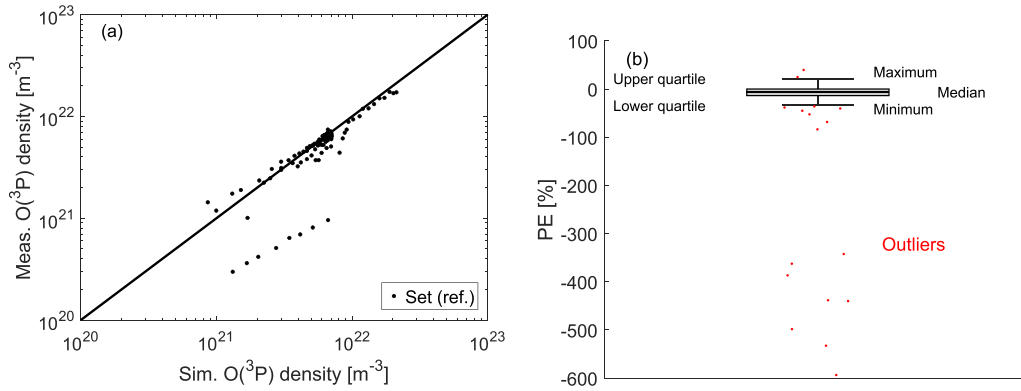


Figure 7. (a) The measured atomic oxygen densities of several μ APPJs from multiple publications [15, 35–38] using the TALIF measurement method versus the corresponding simulated ones of this work using the plug-flow model. The atomic oxygen densities are identical to those in figure 6 excluding the SEA measurement data. The densities are calculated with the reference chemical kinetics (i.e. the reaction ‘Set (ref.)’ reported in appendix A. (b) The box plot visualization of the percentage error between the measured and simulated atomic oxygen densities in (a). TALIF measurement data with 118 points from 5 publications (i.e. [15] 15, [35] 8, [36] 4, [37] 87 and [38] 4) are included.

overall smaller than the SEA measurement data. Furthermore, the TALIF measurement data being smaller than the SEA ones was recently reported by Steuer *et al* [38]. While the relative accuracy of TALIF and SEA can be debated, TALIF generally involves less assumptions than SEA. For instance, it does not rely on simulations of the EEDF within the jet. Because of this, we assume that the TALIF measurements give a better representation of the atomic oxygen density than the SEA measurements. In view of this, the SEA measurement data are excluded in the following investigation of the model prediction accuracy. Therefore, we focus on the prediction accuracy of the simulations relative to the TALIF measurements.

The majority of the data points using the TALIF in figure 6 are close to the black solid line, while some of the data points using the TALIF are further from the black solid line than the majority likely due to multiple factors. For example, this may be because there is a certain amount of variability between different experimental studies under similar plasma operating conditions, or because the simulations are not a good physical representation of the experimental conditions under which those data were taken. This could be due to discrepancies in the spatial position of measurement and simulation, as discussed earlier, for example. Whatever the specific reason that data may be outlying from an ideal agreement between experiment and simulation, consideration of genuine outliers of this type will skew the distribution of the percentage error between simulation and experiment, leading to difficulties in quantifying the model predictive accuracy in the analysis below. Because of this, it is reasonable to consider excluding genuinely outlying comparisons from the final calculation of the model prediction accuracy. It should be emphasized that including outlying points in the analysis does not influence the qualitative outcomes discussed below and the analysis could also be carried out with the complete dataset. However, a skewed distribution means that averaged metrics of the percentage error distribution become less meaningful. In this context, the identification and exclusion of outliers is

carried out here purely for ease of interpretation of the distributions presented later.

The measured atomic oxygen densities using the TALIF [15, 35–38] versus the corresponding simulated ones using the plug-flow model of this work are presented in figure 7(a). The prediction accuracy of our simulation results relative to the aforementioned TALIF measurement data is quantified by the percentage error straightforwardly providing the degree of underprediction and overprediction [46]. The percentage error is given by

$$\text{percentage error (PE)} = \frac{n_{\text{meas.}}(i) - n_{\text{sim.}}(i)}{n_{\text{meas.}}(i)} \cdot 100\%, \quad (2)$$

where $n_{\text{meas.}}(i)$ and $n_{\text{sim.}}(i)$ are the measured and simulated atomic oxygen densities of a certain data point i , respectively. A box plot of the percentage error between the measured and simulated atomic oxygen densities in figure 7(a) is visualized in figure 7(b). The box plot as a simple and straightforward detection technique [74–77] provides a boundary to visually pinpoint outliers. The boundary is defined at a minimum and a maximum which are away from the lower quartile and the upper quartile for $1.5 \times$ distance between the lower and upper quartiles, respectively [74, 76], where the lower quartile is the 25th percentile and the upper quartile is the 75th percentile. The data points outside the minimum and maximum are regarded as the outliers. It is found in figure 7(b) that eight data points located in the range of $-600\% - 300\%$ are significantly far away from the minimum. Therefore, these eight data points are treated as significant outliers, and excluded in the following investigation of the model prediction accuracy relative to the TALIF measurements. On the other hand, there are also some other data points outside the minimum and maximum, which are also defined as outliers by the box plot method. However these data points are much closer to the minimum and maximum compared to the aforementioned eight data points. Furthermore, these data points are part of the measurement data sets from specific publications, where

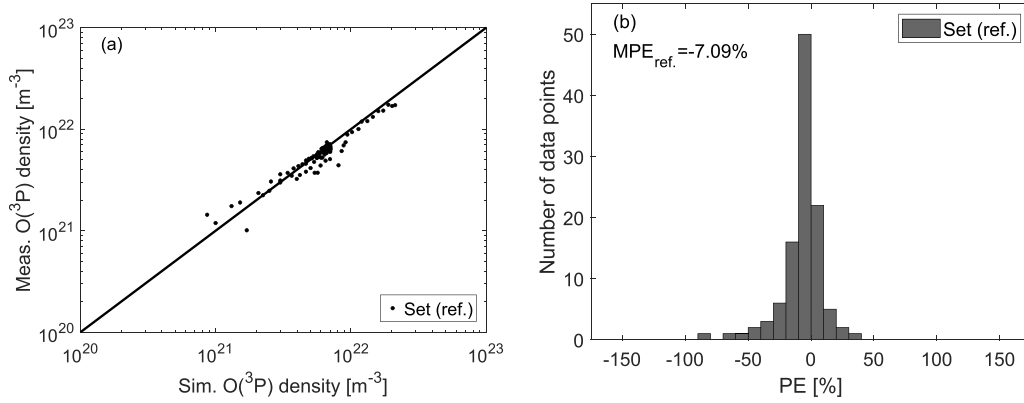


Figure 8. (a) The measured atomic oxygen densities of several μ APPJs from multiple publications [15, 36–38] using the TALIF measurement method versus the corresponding simulated ones of this work using the plug-flow model. The atomic oxygen densities are identical to those in figure 7(a) excluding the eight significant outliers detected by the box plot in figure 7(b). The densities are calculated with the reference chemical kinetics (i.e. the reaction ‘Set (ref.)’) reported in appendix A. (b) The histogram visualization of the number of data points versus the percentage error of the measured and simulated atomic oxygen densities in (a). TALIF measurement data with 110 points from 4 publications (i.e. [15] 15, [36] 4, [37] 87 and [38] 4) are included.

Table 3. The first three dominant gain and loss reaction channels of the atomic oxygen species O(³P) and their corresponding contribution at the plasma channel exit of the COST-Jet under a typical operating condition, i.e. 1000 sccm He mixed with 0.5% O₂ is fed into the plasma channel driven by the absorbed power of 1.00 W. ‘O₂’ in this table represents O₂(X, v = 0). The results are obtained from the plug-flow model calculations using the reference chemical kinetics (i.e. the reaction ‘Set (ref.)’) reported in appendix A.

#	Reaction	Contribution	Tables
Dominant gain reaction channels of O(³ P)			
1	$e + \text{O}_2 \rightarrow e + 2\text{O}(\text{}^3\text{P})$	28.72%	A2(R9)
2	$\text{O}_2(b^1\Sigma_g^+) + \text{O}_3 \rightarrow 2\text{O}_2 + \text{O}(\text{}^3\text{P})$	20.62%	A3(R11)
3	$e + \text{O}_2 \rightarrow e + \text{O}(\text{}^1\text{D}) + \text{O}(\text{}^3\text{P})$	14.49%	A2(R10)
Dominant loss reaction channels of O(³ P)			
4	$\text{O}(\text{}^3\text{P}) + \text{wall} \rightarrow 1/2\text{O}_2$	34.78%	A6(R14)
5	$\text{He} + \text{O}(\text{}^3\text{P}) + \text{O}_2 \rightarrow \text{He} + \text{O}_3$	26.20%	A2(R95)
6	$\text{He} + 2\text{O}(\text{}^3\text{P}) \rightarrow \text{He} + \text{O}_2(b^1\Sigma_g^+)$	13.09%	A3(R86)

most of the measurement data are not defined as outliers. In view of this, these data points are still included in the following investigation of the model prediction accuracy relative to the TALIF measurements, even though they have been identified as outliers.

The atomic oxygen densities [15, 36–38] in figure 8(a) are identical to those in figure 7(a) excluding the eight significant outliers detected by the box plot in figure 7(b). An intuitive distribution of the percentage error (i.e. the degree of underprediction and overprediction) can be given by a histogram plot. Therefore, the histogram plot is visualized in figure 8(b) with the number of the data points versus the percentage error of the measured and simulated atomic oxygen densities in figure 8(a). As expected, an approximate normal distribution of the percentage error is observed in the histogram plot of figure 8(b), and most of the values are close to 0%. In addition, the mean percentage error [46] is used in this work to provide one single value describing the model prediction accuracy relative to all the measurement data [15, 36–38]. The mean percentage error is calculated by

mean percentage error (MPE)

$$= \frac{1}{L} \sum_{i=1}^L \frac{n_{\text{meas.}}(i) - n_{\text{sim.}}(i)}{n_{\text{meas.}}(i)} \cdot 100\%, \quad (3)$$

where L is the number of the data points. The mean percentage error in the case of the simulations using the reaction ‘Set (ref.)’ is $\text{MPE}_{\text{ref.}} = -7.09\%$, close to 0%. This $\text{MPE}_{\text{ref.}}$ value is obtained in the case of excluding all SEA measurement data in figure 6 and 8 TALIF data points in figure 7. However, this still quantitatively indicates that the atomic oxygen densities of the μ APPJs measured by various research groups [15, 36–38] using the TALIF method (i.e. the remaining 110 TALIF data points) can be well predicted by the model of this work.

5.3. Role of important gain and loss channels for atomic oxygen

The first three dominant atomic oxygen gain and loss reaction channels and their corresponding contribution at the plasma channel exit of the COST-Jet are reported in table 3. As noted

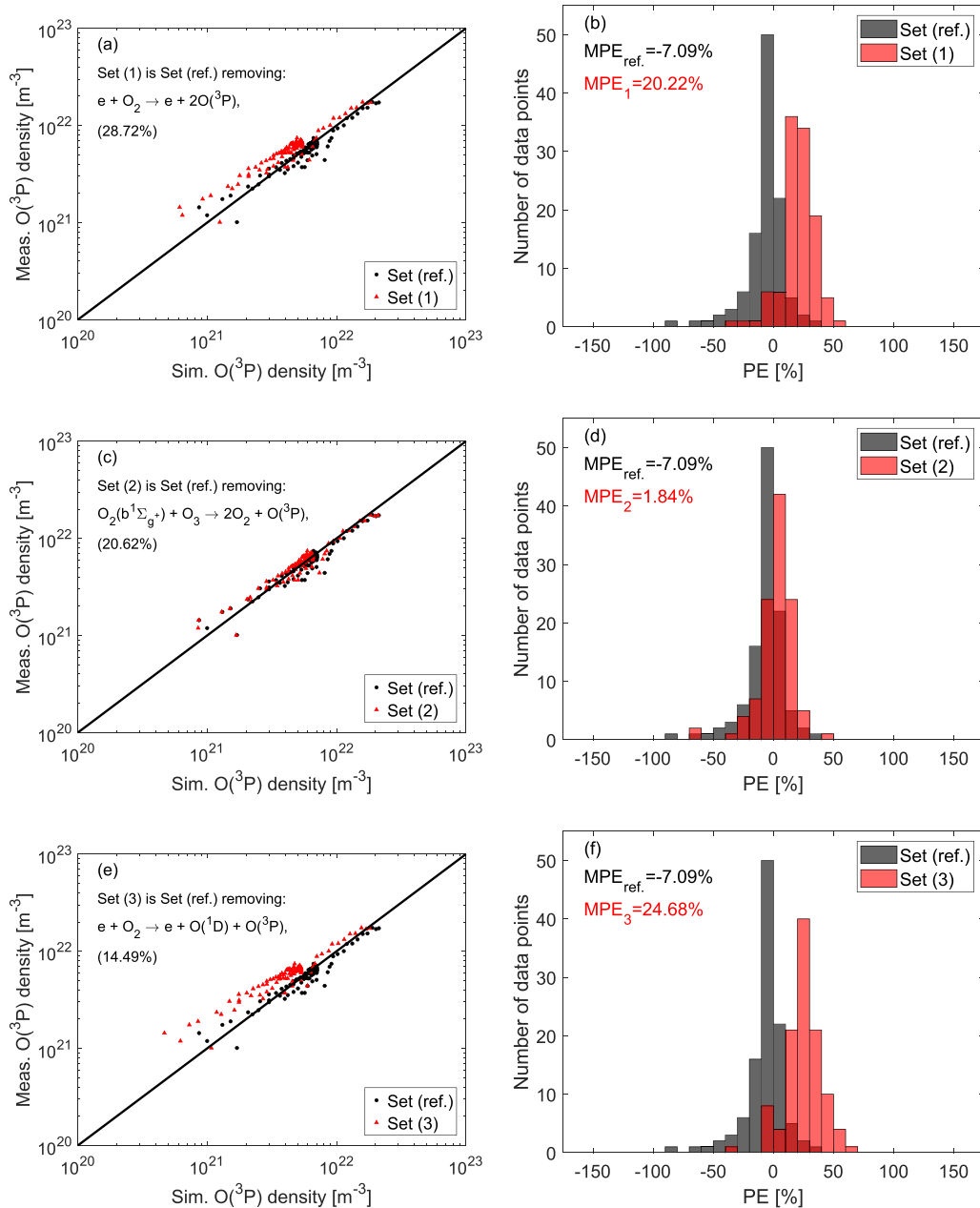


Figure 9. The influence of removing each of the dominant atomic oxygen gain reaction channels (1), (2) and (3) in table 3 in the simulations on our model prediction accuracy relative to the TALIF measurements from multiple publications [15, 36–38]. The measured atomic oxygen densities versus the corresponding simulated ones and the histogram visualization of the corresponding percentage error using the reaction ‘Set (1)’, ‘Set (2)’ or ‘Set (3)’ in the simulations are presented in the same way as those using the reaction ‘Set (ref.)’ in the simulations in figures 8(a) and (b), respectively. The reaction ‘Set (ref.)’ are the reference chemical kinetics reported in appendix A. The reactions ‘Set (1)’ in figures (a)–(b), ‘Set (2)’ in figures (c)–(d) and ‘Set (3)’ in figures (e)–(f) are the reaction ‘Set (ref.)’ removing reactions (1), (2) and (3) in table 3, respectively.

earlier, one focus of this work is dedicated to analyzing the influence of an absence of the dominant atomic oxygen gain and loss reaction channels on our model prediction accuracy. Specifically, the influence of removing each of these dominant reaction channels on the model prediction accuracy is investigated in the following texts. It should be emphasized that the dominant reaction channels and the corresponding contribution vary at different plasma channel positions of the μ APPJs and change with a variation of the operating conditions such as the absorbed power, the He gas flow rate and the O₂ mixture

ratio. An analysis of the full picture of these dominant reaction channels at each plasma channel position and each operating condition deviates from our main focus: i.e. the model prediction accuracy mentioned above. For the sake of the simplicity, only the dominant reaction channels at the plasma channel exit of the COST-Jet under the typical operating condition in table 3 are analyzed.

The influence of removing each of the dominant atomic oxygen gain reaction channels in table 3 in the simulations on our model prediction accuracy are presented in figure 9. It is

found in figures 9(a), (c) and (e) that most of the atomic oxygen density data points in the case of using the reaction ‘Set (ref.)’ are evenly distributed on both sides of the black solid line, while those using the reactions ‘Set (1)’, ‘Set (2)’ and ‘Set (3)’ are above the black solid line. The influence of the dominant gain reaction channels on the model prediction accuracy is illustrated more clearly in figures 9(b), (d) and (f). The percentage error histogram plot in the case of using the reaction ‘Set (ref.)’ is approximately a normal distribution with a mean of -7.09% , while the means of the approximate normal distributions in the case of using the reactions ‘Set (1)’, ‘Set (2)’ and ‘Set (3)’ are shifted to the right and to be positive values of 20.22% , 1.84% and 24.68% , respectively. In other words, the simulation results in the case of removing one of the dominant atomic oxygen gain reaction channels overall underestimate the measurement data in figure 9. This is ascribed to the lower production rate of atomic oxygen in the case of the absence of a corresponding dominant gain reaction channel in the simulations.

It is observed in figure 9 that the degree to which the mean percentage error is shifted is not directly correlated with the contribution of the corresponding dominant atomic oxygen gain reaction channel. For instance, the second dominant reaction channel $O_2(b^1\Sigma_g^+) + O_3 \rightarrow 2O_2 + O(^3P)$ contributes 20.62% of atomic oxygen production. However, the mean percentage error is only shifted by $MPE_2 - MPE_{ref.} = 1.84\% - (-7.09\%) = 8.93\%$ in the simulations removing this dominant reaction channel. In contrast, the third dominant reaction channel $e + O_2 \rightarrow e + O(^1D) + O(^3P)$ contributes 14.49% of atomic oxygen production, but the mean percentage error is even shifted by $MPE_3 - MPE_{ref.} = 24.68\% - (-7.09\%) = 31.77\%$ in the simulations excluding this dominant reaction. It should be emphasized that this non-correlation is potentially caused by diverse factors, e.g. including but not limited to the following three points. (i) As noted earlier, the dominant reaction channels and especially the corresponding contribution vary at different plasma channel position of the μ APPJs and change with a variation of the operating conditions such as the absorbed power, the He gas flow rate and the O_2 mixture ratio. (ii) The number of the corresponding data points at different plasma channel positions under different operating conditions involved in this work deviates from each other. (iii) The corresponding complex chemical kinetics defining the atomic oxygen density at certain plasma channel positions under certain operating conditions are affected by the absence of an associated dominant reaction channel, e.g. the calculated $O_2(b^1\Sigma_g^+)$ and O_3 densities are likely affected by removing reactions (2), (5) and (6) in table 3 in the simulations, which may increase the influence of other reaction channels involving these two species on the production or destruction of the atomic oxygen.

It is observed in figure 9 that the mean percentage error in the case of using ‘Set (2)’ (i.e. 1.84%) is closer to 0% compared to that using ‘Set (ref.)’ (i.e. -7.09%), for the measured atomic oxygen densities under the corresponding operating conditions considered in the current work. This does not

imply that ‘Set (2)’ provides a more accurate description of the atomic oxygen reaction kinetics compared to those using ‘Set (ref.)’, since the importance of a particular reaction channel for the model prediction accuracy in terms of the mean percentage error is determined by diverse factors such as the points (i), (ii) and (iii) of the non-correlation mentioned above. In this sense, optimising the reaction scheme or the model purely to minimise the MPE between measured and simulated atomic oxygen densities, or any other metric comparing experiment and simulation, does not necessarily lead to a better model. This will be an important point to consider if such metric are to be used as part of systematic model optimisation studies, particularly if machine learning approaches with minimal supervision are used. The risks of such overfitting could be mitigated where data on the measurements of multiple species are available, such that individual MPEs could be defined for each species. In such cases, a more complete view of the level of agreement between experiment and simulation would be obtained as opposed to the comparisons with a single reference metric that is carried out here.

The influence of removing each of the dominant atomic oxygen loss reaction channels in table 3 in the simulations on our model prediction accuracy are presented in figure 10. The above-mentioned outcomes in figure 9 are similarly obtained in figure 10. The exception is that three reaction sets, i.e. ‘Set (4)’, ‘Set (5)’ and ‘Set (6)’, are obtained by removing reactions (4), (5) and (6) in table 3 in the reaction ‘Set (ref.)’, respectively. Most of the atomic oxygen density data points using the reactions ‘Set (4)’, ‘Set (5)’ and ‘Set (6)’ are under the black solid line, and the means of the approximate normal distributions of the corresponding percentage error are shifted to the left and to the negative values of -40.71% , -13.06% and -16.20% , respectively. In other words, the simulation results in the case of removing one of the dominant atomic oxygen loss reaction channels overall overestimate the measurement data in figure 10. This is owing to the lower destruction rate of atomic oxygen in the case of the absence of a corresponding dominant loss reaction channel in the simulations. Similar non-correlation is obtained between the shifted degree of the mean percentage error and the contribution of the corresponding dominant atomic oxygen loss reaction channel, due to the potential causes mentioned above.

The above-mentioned percentage error distributions of the measured and simulated atomic oxygen densities in figures 8–10 are summarized in figure 11 with the violin plot [78], which combines the advantages of the above-mentioned box plot (see figure 7(b)) and histogram plot (see figure 8(b)). Specifically, each violin consists of a white spot denoting the median, a gray bar representing the range of the lower and upper quartiles, and a gray line showing the region between the minimum and maximum. The width of the violin provides the relative distribution of the percentage error. It is intuitively and quantitatively observed that the percentage errors are shifted in the positive direction in the simulations using the reactions ‘Set (1)’, ‘Set (2)’ and ‘Set (3)’, while the percentage errors are shifted in the negative direction in the simulations using the

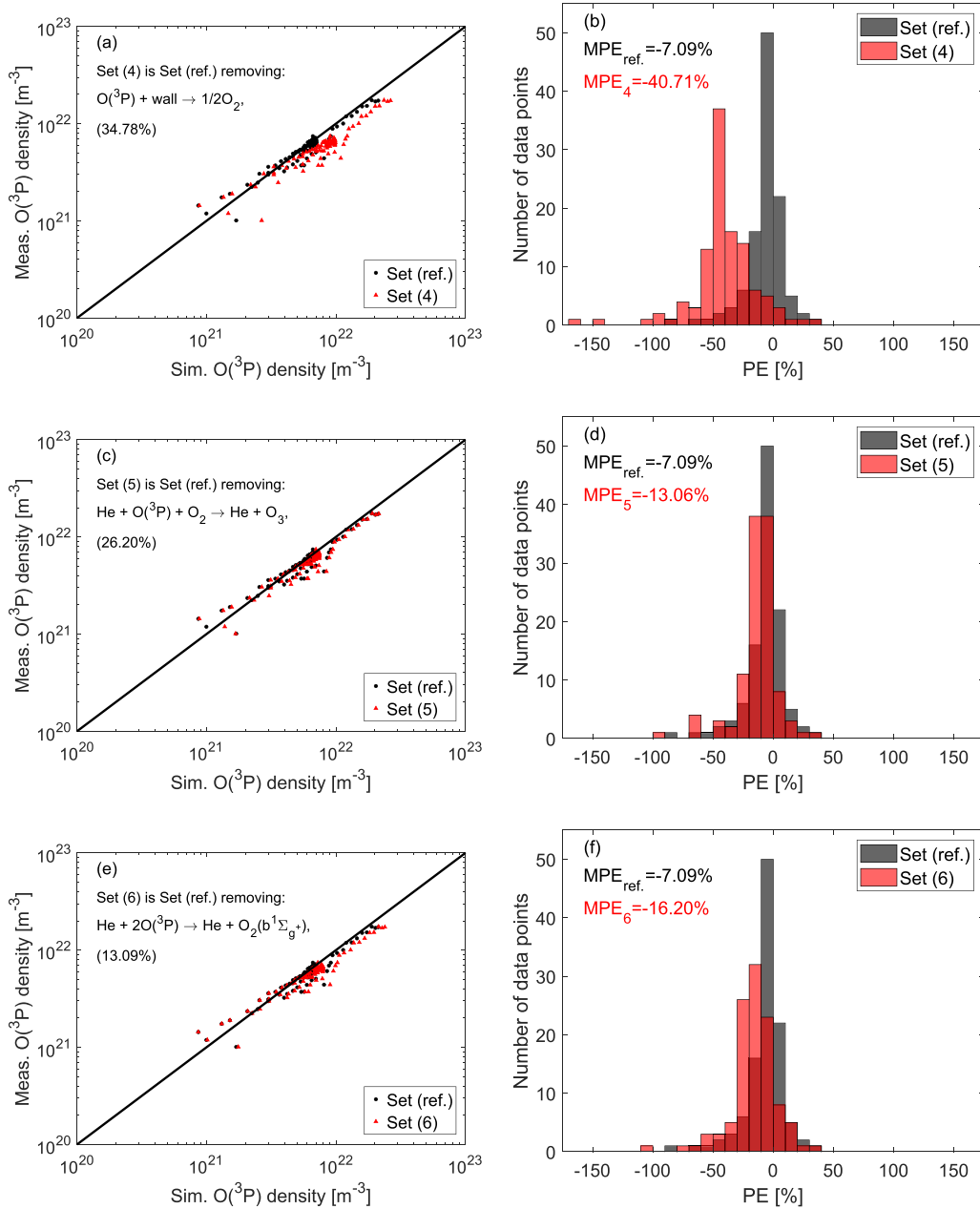


Figure 10. As in figure 9, but the dominant atomic oxygen loss reactions (4), (5) and (6) in table 3 are removed from the reaction ‘Set (ref.)’ to be the reaction ‘Set (4)’, ‘Set (5)’ and ‘Set (6)’, respectively.

reactions ‘Set (4)’, ‘Set (5)’ and ‘Set (6)’ compared to those using the reaction ‘Set (ref.)’. In other words, the simulation results in the case of removing a dominant atomic oxygen gain reaction channel in the simulations overall underestimate the

measurement data, while the simulation results in the case of removing a dominant atomic oxygen loss reaction channel in the simulations overall overestimate the measurement data.

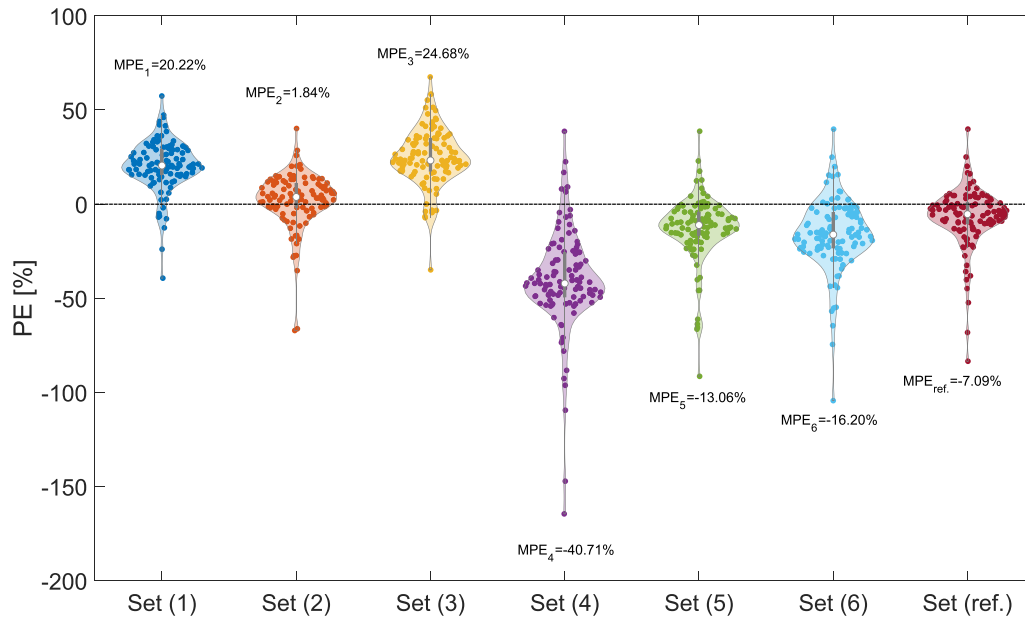


Figure 11. The violin plot visualization [78] of the percentage error distributions of the measured and simulated atomic oxygen densities obtained in the simulations using the reactions ‘Set (ref.)’, ‘Set (1)’, ‘Set (2)’, ‘Set (3)’, ‘Set (4)’, ‘Set (5)’ and ‘Set (6)’ in figures 8(b), 9(b), (d), (f), 10(b), (d) and (f), respectively. The violin plot is used to summarize the distributions of the percentage error provided in the aforementioned figures. For further details of the violin plot, see texts.

6. Conclusion

The simulated atomic oxygen densities using the plug-flow model of this work are validated against the measured ones of the parallel plate radio frequency driven He/O₂ μ APPJs reported in a range of publications [15, 33–39] using different measurement methods. These publications are from several research groups. These μ APPJs are the COST-Jet [35–38], the COST-Jet prototype [15, 33, 34], and the μ APPJ similar to the COST-Jet [39]. It is worth to note that non-reproducibility of the measurement data due to the gas contamination and the absorbed power uncertainty was minimized by the COST-Jet [32]. The measurement data of the aforementioned μ APPJs are as a function of the absorbed power (0.06–6.50 W), the He gas flow rate (200–1500 sccm), and the O₂ mixture ratio (0.1%–2.0%). They were collected along the gas flow direction in the plasma channel region, at the middle or exit of the plasma channel region, and in the near effluent region at 1 mm distance from the plasma channel exit. The measurement methods include the TALIF, the SEA, and the OES supported by numerical simulations. For further specific details of how model and experiment are compared, see sections 2 and 3. Generally good agreement between the simulated atomic oxygen densities and a large fraction of the experimental data points is obtained. Particularly good agreement is achieved between the simulations and the majority of the TALIF measurement data points. On the other hand, the measurements by SEA generally give larger atomic oxygen densities than the equivalent TALIF measurements, and the simulations.

Our model prediction accuracy relative to the measurements from various publications is quantified by the percentage error between the measured and simulated atomic oxygen densities. In the study of the prediction accuracy, a total of

174 data points are considered: i.e. 118 TALIF measurements from 5 publications [15, 35–38] and 56 SEA data points from 2 publications [38, 39]. Based on the fact that the SEA data is systematically larger than equivalent TALIF measurements, and our simulations, the SEA measurement data are excluded from the investigation of the model prediction accuracy. Furthermore, 8 TALIF data points are excluded, as they are detected as significant outliers based on a box plot of the percentage error. The percentage error between the remaining 110 TALIF data points [15, 36–38] and our simulation results is visualized with the histogram plot to present its distribution intuitively. As expected, an approximate normal distribution is observed, and the mean percentage error is close to zero. This slight positive and negative deviation between the measurements and simulations is due to diverse factors such as model limitation, experimental error, and potential inconsistency between the input parameters of measurements and simulations.

The influence of removing one of the dominant atomic oxygen gain and loss reaction channels in the simulations on our model prediction accuracy relative to the above-mentioned TALIF measurements [15, 36–38] is analyzed. In the analysis, only the first three dominant gain and loss reaction channels at the plasma channel exit of the COST-Jet under a typical operating condition are considered for the sake of simplicity. The mean of the approximate normal distribution of the percentage error is shifted positively and negatively in the case of removing a dominant gain and loss reaction channel, which means the simulation results overall underestimate and overestimate the measurement data, respectively. These shifts are intuitively presented in a violin plot. The shift degree of the mean percentage error is not directly correlated with the contribution of the corresponding dominant reaction channel due to diverse factors: such as the different contribution of the

dominant reaction channel at different plasma channel position under different operating condition, the number of the corresponding data points involved, and the convoluted chemical kinetics of the atomic oxygen altered by the absence of a corresponding dominant reaction channel. However, the observations in this work still indicate that incorporation of the dominant reaction channels in the simulations has a significant effect on their predictive capabilities, and that this can be quantified by the mean percentage error.

The validations presented in this work do have a number of limitations that may be improved in future. Firstly, where measurements have been carried out in the near effluent region of the jet they have been compared with simulations at the jet exit in this work. The development of a more refined model of the effluent, including the decrease in the gas flow velocity in this region and the mixing with ambient air, would allow for robust simulations in the effluent. These could then be compared with experimental data at each specific measurement position. This would not only increase the quality of the validation for the near effluent, but would also increase the amount of data that could be effectively compared with the model to include studies where the spatial variation of densities in the effluent have been measured. Another important area for future work would be the inclusion of both uncertainties in both measurements and model into the validation analysis. While these have been discussed in this work, they could also be formally included in the analysis, in principle. From the point of view of the simulations, the atomic oxygen wall recombination probability is a key uncertainty, which may be improved by the inclusion of a surface kinetics model. However, each rate coefficient in the model is subject to an uncertainty, and the overall uncertainty in the atomic oxygen density predicted by the model is not only related to the atomic oxygen surface recombination probability. As such, future work in this area should also include the quantification of simulated uncertainties using the approach proposed by Turner [22], or similar.

Overall, a framework has been presented via which simulation results can be quantitatively compared to measurement data under a variety of operating conditions. The distribution of the percentage error and the corresponding mean percentage error are intuitive metrics for comparing experiment and simulation, when there are a sufficient number of measurement data available. The COST-Jet, and other sources related to it, provide an ideal platform for such comparisons, due to their reproducibility and the wide range of measurement data that have been carried out on them by multiple research groups. Future work in this area may include the use of such comparisons for the optimization of chemical kinetics schemes, potentially using machine learning approaches, based on minimization of the mean percentage error, while keeping in mind the need to avoid overfitting. The manual analysis of the quantitative influence of the dominant reaction channels on the model prediction accuracy (in terms of the mean percentage error) shown in the current work provides some guiding principles for such work. Furthermore, the present framework can be used to optimize not only the chemical kinetics of the atomic oxygen studied in the current work but also those of other reactive species in other gas mixtures. It should be noted that a prerequisite for such future studies is availability of a sufficient number of well-defined experimental measurements for the quantities of interest.

Data availability statement

The data that support the findings of this study will be made openly available on the database <https://rdpcidat.rub.de/>.

Acknowledgment

Funded by the Deutsche Forschungsgemeinschaft (DFG, German Research Foundation)–Project-ID 327886311 (SFB 1316: A9).

Appendix A. Chemical kinetics considered in this work including the updates and supplements compared to those in previous work [17]

Table A1. The helium only related volume reactions included in the He/O₂ model. For updates compared to our previous work [17] see notes below the table. The rate coefficient units are given in s⁻¹, m³ s⁻¹ and m⁶ s⁻¹ for one-, two- and three-body reactions, respectively. T_e is in eV and T_g in K, if not stated otherwise. The rate coefficient $f(\epsilon)$ is taken from a look-up-table calculated via the referenced cross-section self-consistently coupled to the EEDF [60]. The reverse reaction rate coefficient of the electron-impact excitation labeled with a symbol ‘*’ near the number is calculated via the principle of *detailed balancing* [59].

#	Reaction	Rate coefficient	References
1	$e + \text{He} \rightarrow 2e + \text{He}^+$	$f(\epsilon)$	[61, 62]
2*	$e + \text{He} \rightarrow e + \text{He}(2^3\text{S})$	$f(\epsilon)$	[61, 62]
3 ^b	$e + \text{He}(2^3\text{S}) \rightarrow 2e + \text{He}^+$	$f(\sigma)$	[79] ^d
4 ^a	$e + \text{He}_2^* \rightarrow e + 2\text{He}$	3.8×10^{-15}	[20, 80]
5 ^b	$e + \text{He}_2^* \rightarrow 2e + \text{He}_2^+$	$f(\sigma)$	[81] ^d
6 ^c	$e + \text{He}^+ \rightarrow \text{He}(2^3\text{S})$	$6.76 \times 10^{-19} T_e^{-0.5}$	[56, 82]
7 ^c	$2e + \text{He}^+ \rightarrow e + \text{He}(2^3\text{S})$	$5.12 \times 10^{-39} T_e^{-4.5}$	[56, 82]
8	$e + \text{He}^+ + \text{He} \rightarrow \text{He}(2^3\text{S}) + \text{He}$	$7.4 \times 10^{-47} (T_e/T_g)^{-2}$	[83]
9 ^c	$e + \text{He}_2^+ \rightarrow \text{He} + \text{He}$	1.0×10^{-14}	[83, 84]
10 ^c	$e + \text{He}_2^+ \rightarrow \text{He}(2^3\text{S}) + \text{He}$	$8.9 \times 10^{-15} (T_e[K]/T_g)^{-1.5}$	[85–87]
11 ^a	$\text{He}^+ + 2\text{He} \rightarrow \text{He}_2^+ + \text{He}$	1.1×10^{-43}	[85–87]
12 ^a	$\text{He}(2^3\text{S}) + 2\text{He} \rightarrow \text{He}_2^* + \text{He}$	2×10^{-46}	[85–87]
13	$\text{He}(2^3\text{S}) + 2\text{He} \rightarrow 3\text{He}$	2×10^{-46}	[83]
14 ^c	$\text{He}(2^3\text{S}) + \text{He}(2^3\text{S}) \rightarrow e + \text{He}_2^+$	$2.03 \times 10^{-15} (T_g/300)^{0.5}$	[83, 88, 89]
15 ^a	$\text{He}(2^3\text{S}) + \text{He}(2^3\text{S}) \rightarrow e + \text{He}^+ + \text{He}$	$8.7 \times 10^{-16} (T_g/300)^{0.5}$	[83, 88, 89]
16 ^a	$\text{He}(2^3\text{S}) + \text{He}_2^* \rightarrow e + \text{He}_2^+ + \text{He}$	2.0×10^{-15}	[80, 83]
17 ^a	$\text{He}(2^3\text{S}) + \text{He}_2^* \rightarrow e + \text{He}^+ + 2\text{He}$	5.0×10^{-16}	[80, 83]
18 ^a	$\text{He}_2^* \rightarrow 2\text{He}$	1×10^4	[86, 87]
19	$\text{He}_2^* + \text{He} \rightarrow 3\text{He}$	1.5×10^{-21}	[83]
20 ^c	$\text{He}_2^* + \text{He}_2^* \rightarrow e + \text{He}_2^+ + 2\text{He}$	1.2×10^{-15}	[80, 83]
21 ^a	$\text{He}_2^* + \text{He}_2^* \rightarrow e + \text{He}^+ + 3\text{He}$	3.0×10^{-16}	[80, 83]

^a Compared to our previous work [17], the ‘Ref’ are updated.

^b Compared to our previous work [17], the ‘Rate coefficient’ is updated.

^c Compared to our previous work [17], the ‘Rate coefficient’ and the ‘Ref’ are updated.

^d The rate coefficient for cases marked with $f(\sigma)$ is directly evaluated according to the calculated EEDF and the corresponding electron-impact cross-section from ‘Ref’.

Table A2. The oxygen related volume reactions in the He/O₂ model. For updates compared to our previous work [17] see notes below the table. ‘O₂’ in this table represents O₂(X, v = 0). M is the background gas helium. The rate coefficient units are given in m³ s⁻¹ and m⁶ s⁻¹ for two- and three-body reactions, respectively. T_e is in eV and T_g in K, if not stated otherwise. The rate coefficient f(ε) is taken from a look-up-table calculated via the referenced cross-section self-consistently coupled to the EEDF [60]. The reverse reaction rate coefficients of the electron-impact excitation labeled with a symbol ‘*’ near the number are calculated via the principle of *detailed balancing* [59].

#	Reaction	Rate coefficient	References
1	$e + O(^3P) + O_2 \rightarrow O^- + O_2$	1×10^{-43}	[90]
2	$e + O(^3P) + O_2 \rightarrow O_2^- + O(^3P)$	1×10^{-43}	[90]
3 ^{*b}	$e + O(^3P) \rightarrow e + O(^1D)$	$f(\sigma)$	[62, 63] ^e
4 ^b	$e + O(^3P) \rightarrow 2e + O^+$	$f(\sigma)$	[62, 63] ^e
5 ^b	$e + O_2 \rightarrow O_2^-$	$f(\sigma)$	[91] ^e
6 ^a	$e + O_2 + O_2 \rightarrow O_2^- + O_2$	$1.4 \times 10^{-41} (T_g/T_e[K]) \exp(-600/T_g) \times \exp\{700(T_e[K] - T_g)/(T_e[K]T_g)\}$	[92, 93]
7 ^b	$e + O_2 + He \rightarrow He + O_2^-$	$3.6 \times 10^{-43} T_e^{-0.5}$	[56]
8	$e + O_2 \rightarrow O^- + O(^3P)$	$f(\epsilon)$	[62, 63]
9	$e + O_2 \rightarrow e + 2O(^3P)$	$f(\epsilon)$	[62, 63]
10	$e + O_2 \rightarrow e + O(^1D) + O(^3P)$	$f(\epsilon)$	[62, 63]
11 ^b	$e + O_2 \rightarrow 2e + O^+ + O(^3P)$	$f(\sigma)$	[79] ^e
12 [*]	$e + O_2 \rightarrow e + O_2(a^1\Delta_g)$	$f(\epsilon)$	[62, 63]
13	$e + O_2 \rightarrow 2e + O_2^+$	$f(\epsilon)$	[62, 63]
14	$e + O_3 + M \rightarrow O_3^- + M$	1×10^{-43}	[90]
15 ^b	$e + O_3 \rightarrow O^- + O_2$	$f(\sigma)$	[94] ^e
16 ^b	$e + O_3 \rightarrow O(^3P) + O_2^-$	$f(\sigma)$	[94] ^e
17 ^c	$e + O_3 \rightarrow e + O(^3P) + O_2$	$f(\sigma)$	[62, 63] ^e
18 ^b	$e + O(^1D) \rightarrow 2e + O^+$	$f(\sigma)$	[95] ^e
19 ^c	$e + O_2(a^1\Delta_g) \rightarrow O(^3P) + O^-$	$f(\sigma)$	[62, 63] ^e
20 ^c	$e + O_2(a^1\Delta_g) \rightarrow e + 2O(^3P)$	$f(\sigma)$	[62, 63] ^e
21 ^c	$e + O_2(a^1\Delta_g) \rightarrow e + O(^3P) + O(^1D)$	$f(\sigma)$	[62, 63] ^e
22 ^c	$e + O_2(a^1\Delta_g) \rightarrow 2e + O(^3P) + O^+$	$f(\sigma)$	[62, 63] ^e
23 ^c	$e + O_2(a^1\Delta_g) \rightarrow 2e + O_2^+$	$f(\sigma)$	[62, 63] ^e
24	$e + e + O^+ \rightarrow e + O(^3P)$	$1 \times 10^{-31} (T_g/T_e[K])^{4.5}$	[96]
25	$e + O^+ + M \rightarrow O(^3P) + M$	$3.12 \times 10^{-35} /T_e[K]^{1.5}$	[96]
26 ^b	$e + O^+ \rightarrow O(^1D)$	$5.3 \times 10^{-19} T_e^{-0.5}$	[56]
27 ^b	$2e + O^+ \rightarrow e + O(^1D)$	$5.12 \times 10^{-39} T_e^{-4.5}$	[56]
28	$e + O_2^+ + M \rightarrow O_2 + M$	$3.12 \times 10^{-35} /T_e[K]^{1.5}$	[96]
29	$e + e + O_2^+ \rightarrow e + O_2$	$1 \times 10^{-31} (T_g/T_e[K])^{4.5}$	[96]
30 ^d	$e + O_2^+ \rightarrow 2O(^3P)$	$0.36 \times 2.2 \times 10^{-14} T_e^{-0.5}$	[69, 97, 98]
31 ^d	$e + O_2^+ \rightarrow O(^1D) + O(^3P)$	$0.64 \times 2.2 \times 10^{-14} T_e^{-0.5}$	[69, 97, 98]
32	$e + O_4^+ \rightarrow O_2 + O_2$	$2.42 \times 10^{-11} /T_e[K]^{0.5}$	[90]
33 ^c	$e + O^- \rightarrow 2e + O(^3P)$	$f(\sigma)$	[62, 63] ^e
34	$He + He^+ + O^- \rightarrow 2He + O(^3P)$	$2 \times 10^{-37} (300/T_g)^{2.5}$	[56]
35	$He + O(^3P) + O^+ \rightarrow He + O_2^+$	$1 \times 10^{-41} (300/T_g)^{-0.5}$	[56]
36	$He + O^- + O^+ \rightarrow He + 2O(^3P)$	$2 \times 10^{-37} (300/T_g)^{2.5}$	[56]
37	$He + O^- + O_2^+ \rightarrow He + O(^3P) + O_2$	$2 \times 10^{-37} (300/T_g)^{2.5}$	[56]
38	$He^+ + O(^3P) \rightarrow He + O^+$	$5 \times 10^{-17} (300/T_g)^{-0.5}$	[56]
39	$He^+ + O_2 \rightarrow He + O(^3P) + O^+$	$1.07 \times 10^{-15} (300/T_g)^{-0.5}$	[56]
40	$He^+ + O_2 \rightarrow He + O_2^+$	$3.3 \times 10^{-17} (300/T_g)^{-0.5}$	[56]
41	$He^+ + O_3 \rightarrow He + O^+ + O_2$	$1.07 \times 10^{-15} (300/T_g)^{-0.5}$	[56]
42	$He^+ + O(^1D) \rightarrow He + O^+$	$5 \times 10^{-17} (300/T_g)^{-0.5}$	[56]
43	$He^+ + O_2(a^1\Delta_g) \rightarrow He + O(^3P) + O^+$	$1.07 \times 10^{-15} (300/T_g)^{-0.5}$	[56]
44	$He^+ + O_2(a^1\Delta_g) \rightarrow He + O_2^+$	$3.3 \times 10^{-17} (300/T_g)^{-0.5}$	[56]
45 ^b	$O^+ + O(^3P) + O_2 \rightarrow O_2 + O_2^+$	$1 \times 10^{-41} (300/T_g)^{-0.5}$	[56]
46 ^d	$O^+ + O_2 \rightarrow O(^3P) + O_2^+$	$2 \times 10^{-17} (300/T_g)^{0.5}$	[99]
47 ^d	$O^+ + O_3 \rightarrow O_2 + O_2^+$	1×10^{-16}	[96]
48	$O_2^+ + O_2 + M \rightarrow O_4^+ + M$	$5.5 \times 10^{-43} (300/T_g)^{2.7}$	[100]
49	$O_4^+ + O(^3P) \rightarrow O_2^+ + O_3$	3×10^{-16}	[96]
50	$O_4^+ + O_2 \rightarrow O_2^+ + O_2 + O_2$	$3.3 \times 10^{-12} (300/T_g)^4 \exp(-5030/T_g)$	[96]
51 ^d	$O^- + O(^3P) \rightarrow e + O_2$	1.3×10^{-15}	[101]
52	$O_2^- + O_2 \rightarrow O_2 + O_2 + e$	$2.7 \times 10^{-16} (T_g/300)^{0.5} \exp(-5590/T_g)$	[90]

(Continued.)

Table A2. (Continued.)

#	Reaction	Rate coefficient	References
53 ^d	$O^- + O_2 \rightarrow e + O_3$	1×10^{-18}	[101]
54	$O^- + O_2 + M \rightarrow O_3^- + M$	$1.1 \times 10^{-42} (300/T_g)$	[90]
55	$O^- + O_2 + O^+ \rightarrow 2O(^3P) + O_2$	$2 \times 10^{-37} (300/T_g)^{2.5}$	[56]
56	$O^- + O_2 + O_2^+ \rightarrow O(^3P) + 2O_2$	$2 \times 10^{-37} (300/T_g)^{2.5}$	[56]
57	$O^- + O_2 + O_2^+ \rightarrow O_2 + O_3$	$2 \times 10^{-37} (300/T_g)^{2.5}$	[59]
58	$O^- + O_3 \rightarrow e + 2O_2$	$3.01 \times 10^{-16} (300/T_g)^{-0.5}$	[56]
59	$O^- + O_3 \rightarrow O(^3P) + O_3^-$	$1.99 \times 10^{-16} (300/T_g)^{-0.5}$	[56]
60	$O^- + O_3 \rightarrow O_2 + O_2^-$	$1.02 \times 10^{-17} (300/T_g)^{-0.5}$	[56]
61 ^d	$O^- + O_2(a^1\Delta_g) \rightarrow e + O_3$	$0.75 \times 1.9 \times 10^{-16}$	[99]
62	$O^- + O_2(a^1\Delta_g) \rightarrow O(^3P) + O_2^-$	1×10^{-16}	[33]
63	$O_2^- + O(^3P) \rightarrow O_2 + O^-$	$1.5 \times 10^{-16} (300/T_g)^{-0.5}$	[56]
64	$O_2^- + O(^3P) \rightarrow e + O_3$	$1.5 \times 10^{-16} (300/T_g)^{-0.5}$	[56]
65 ^a	$O_2^- + O_2 + M \rightarrow O_4^- + M$	$3.5 \times 10^{-43} (300/T_g)$	[96]
66	$O_2^- + O_3 \rightarrow O_2 + O_3^-$	$6 \times 10^{-16} (300/T_g)^{-0.5}$	[56]
67	$O_2^- + O_3 \rightarrow O_3 + O_2 + e$	6×10^{-16}	[102]
68 ^b	$O_2^- + O_2(a^1\Delta_g) \rightarrow e + 2O_2$	$2 \times 10^{-16} (300/T_g)^{-0.5}$	[56]
69	$O_3^- + O(^3P) \rightarrow O_2 + O_2^-$	$2.5 \times 10^{-16} (300/T_g)^{-0.5}$	[56]
70	$O_3^- + O(^3P) \rightarrow O_2 + O_2 + e$	3×10^{-16}	[90]
71	$O_3^- + O_2 \rightarrow O_3 + O_2 + e$	2.3×10^{-17}	[102]
72	$O_3^- + O_3 \rightarrow O_2 + O_2 + O_2 + e$	3×10^{-16}	[102]
73	$O_4^- + O(^3P) \rightarrow O^- + O_2 + O_2$	3×10^{-16}	[90]
74	$O_4^- + O(^3P) \rightarrow O_3^- + O_2$	4×10^{-16}	[90]
75	$He^+ + O^- \rightarrow He + O(^3P)$	$2 \times 10^{-13} (300/T_g)$	[56]
76	$He^+ + O_2^- \rightarrow He + O_2$	$2 \times 10^{-13} (300/T_g)$	[56]
77	$He^+ + O_3^- \rightarrow He + O_3$	$2 \times 10^{-13} (300/T_g)$	[56]
78 ^d	$O^+ + O^- \rightarrow 2O(^3P)$	2.8×10^{-13}	[103]
79	$O^+ + O_2^- \rightarrow O(^3P) + O_2$	$2 \times 10^{-13} (300/T_g)$	[56]
80	$O^+ + O_3^- \rightarrow O(^3P) + O_3$	$2 \times 10^{-13} (300/T_g)$	[56]
81	$O^+ + O_4^- \rightarrow O_2 + O_2 + O(^3P)$	1×10^{-13}	[90]
82	$O_2^+ + O^- \rightarrow 3O(^3P)$	1×10^{-13}	[56]
83 ^d	$O_2^+ + O^- \rightarrow O(^3P) + O_2$	$9.6 \times 10^{-14} (300/T_g)^{0.5}$	[99]
84	$O_2^+ + O_2^- \rightarrow 2O(^3P) + O_2$	1×10^{-13}	[56]
85	$O_2^+ + O_2^- \rightarrow 2O_2$	$2 \times 10^{-13} (300/T_g)$	[56]
86 ^b	$O_2^+ + O_3^- \rightarrow 2O(^3P) + O_3$	1×10^{-13}	[56]
87	$O_2^+ + O_3^- \rightarrow O_2 + O_3$	$2 \times 10^{-13} (300/T_g)$	[56]
88	$O_2^+ + O_4^- \rightarrow O_2 + O_2 + O_2$	1×10^{-13}	[90]
89	$O_4^+ + O^- \rightarrow O(^3P) + O_2 + O_2$	1×10^{-13}	[90]
90	$O_4^+ + O_2^- \rightarrow O_2 + O_2 + O_2$	1×10^{-13}	[90]
91	$O_4^+ + O_3^- \rightarrow O_3 + O_2 + O_2$	1×10^{-13}	[90]
92	$O_4^+ + O_4^- \rightarrow O_2 + O_2 + O_2 + O_2$	1×10^{-13}	[90]
93	$He + 2O(^3P) \rightarrow He + O_2$	1×10^{-45}	[56]
94	$He + 2O(^3P) \rightarrow He + O_2(a^1\Delta_g)$	$9.88 \times 10^{-47} (300/T_g)^{0.63}$	[56]
95	$He + O(^3P) + O_2 \rightarrow He + O_3$	$3.4 \times 10^{-46} (300/T_g)^{1.2}$	[56]
96	$He + O(^1D) \rightarrow He + O(^3P)$	1×10^{-19}	[56]
97	$He + O_2(a^1\Delta_g) \rightarrow He + O_2$	$8 \times 10^{-27} (300/T_g)^{-0.5}$	[56]
98	$He(2^3S) + O(^3P) \rightarrow He + O^+ + e$	$2.54 \times 10^{-16} (300/T_g)^{-0.5}$	[56]
99	$He(2^3S) + O_2 \rightarrow He + O_2^+ + e$	$2.54 \times 10^{-16} (300/T_g)^{-0.5}$	[56]
100	$He(2^3S) + O_3 \rightarrow He + O(^3P) + O_2^+ + e$	$2.54 \times 10^{-16} (300/T_g)^{-0.5}$	[56]
101	$He(2^3S) + O(^1D) \rightarrow He + O^+ + e$	$2.54 \times 10^{-16} (300/T_g)^{-0.5}$	[56]
102	$He_2^* + O_2 \rightarrow e + 2He + O_2^+$	3.6×10^{-16}	[104, 105]
103 ^d	$3O(^3P) \rightarrow O(^3P) + O_2$	$2.5 \times 10^{-43} T_g^{-0.63}$	[106]
104	$3O(^3P) \rightarrow O(^3P) + O_2(a^1\Delta_g)$	$6.93 \times 10^{-47} (300/T_g)^{0.63}$	[56]
105 ^d	$O(^3P) + 2O_2 \rightarrow O_2 + O_3$	$0.33 \times 6.4 \times 10^{-47} \exp(663/T_g)$	[99, 107]
106 ^d	$2O(^3P) + O_2 \rightarrow O(^3P) + O_3$	$2.1 \times 10^{-46} \exp(345/T_g)$	[99]
107 ^d	$2O(^3P) + O_2 \rightarrow 2O_2$	$0.5 \times 3.81 \times 10^{-42} T_g^{-1} \exp(-170/T_g)$	[99, 108]
108 ^d	$2O(^3P) + O_2 \rightarrow O_2 + O_2(a^1\Delta_g)$	$0.33 \times 3.81 \times 10^{-42} T_g^{-1} \exp(-170/T_g)$	[99, 108]
109 ^d	$O(^3P) + O_2 + O_3 \rightarrow 2O_3$	$1.66 \times 10^{-46} \exp(T_g/300)$	[109]

(Continued.)

Table A2. (Continued.)

110	$O(^3P) + O_3 \rightarrow 2O(^3P) + O_2$	$1.56 \times 10^{-15} \exp(-11490/T_g)$	[56]
111 ^d	$O(^3P) + O_3 \rightarrow 2O_2$	$0.5 \times 1.8 \times 10^{-17} \exp(-2300/T_g)$	[99, 108]
112	$O_2 + O_3 \rightarrow O(^3P) + 2O_2$	$1.56 \times 10^{-15} \exp(-11490/T_g)$	[56]
113	$2O_3 \rightarrow O(^3P) + O_2 + O_3$	$1.56 \times 10^{-15} \exp(-11490/T_g)$	[56]
114	$O_3 + M \rightarrow O(^3P) + O_2 + M$	$3.92 \times 10^{-16} \exp(-11400/T_g)$	[110]
115 ^d	$O(^1D) + O(^3P) \rightarrow 2O(^3P)$	8×10^{-18}	[99]
116 ^d	$O(^1D) + O_2 \rightarrow O(^3P) + O_2$	$7 \times 10^{-18} \exp(67/T_g)$	[99]
117 ^d	$O(^1D) + O_2 \rightarrow O(^3P) + O_2(a^1\Delta_g)$	$8 \times 10^{-19} \exp(67/T_g)$	[111, 112]
118 ^d	$O(^1D) + O_3 \rightarrow 2O(^3P) + O_2$	1.2×10^{-16}	[99]
119 ^d	$O(^1D) + O_3 \rightarrow 2O_2$	1.2×10^{-16}	[99]
120 ^a	$O(^1D) + O_2(a^1\Delta_g) \rightarrow O(^3P) + O_2$	1×10^{-17}	[92, 113]
121 ^d	$O_2(a^1\Delta_g) + O(^3P) \rightarrow O(^3P) + O_2$	7×10^{-22}	[96, 114]
122 ^b	$O_2(a^1\Delta_g) + O_2 \rightarrow O(^3P) + O_3$	$2.95 \times 10^{-27} (300/T_g)^{-0.5}$	[56]
123 ^d	$O_2(a^1\Delta_g) + O_2 \rightarrow 2O_2$	$2.2 \times 10^{-24} (T_g/300)^{0.8}$	[96]
124 ^d	$O_2(a^1\Delta_g) + O_3 \rightarrow O(^3P) + 2O_2$	$5.2 \times 10^{-17} \exp(-2840/T_g)$	[99, 112]
126	$2O_2(a^1\Delta_g) \rightarrow 2O_2$	$9 \times 10^{-23} \exp(-560/T_g)$	[56]

^a Compared to our previous work [17], the ‘Ref’ is updated.

^b Compared to our previous work [17], the ‘Rate coefficient’ is updated.

^c Compared to our previous work [17], the ‘Rate coefficient’ and the ‘Ref’ are updated.

^d Compared to our previous work [17], the ‘Rate coefficient’ and the ‘Ref’ are updated based on the work of Dias *et al* [64]. For Reactions 47, 115, 118, 119 and 124, only the ‘Ref’ is updated.

^e The rate coefficient for cases marked with $f(\sigma)$ is directly evaluated according to the calculated EEDF and the corresponding electron-impact cross-section from ‘Ref’.

Note: Reaction 125: $O_2(a^1\Delta_g) + O_3 \rightarrow O(^1D) + 2O_2$ with a rate coefficient of $1.01 \times 10^{-17} \text{ m}^3 \text{ s}^{-1}$ that was used in [17] (P. 24) is deleted in the current work. The rate coefficient of Reaction 125 is much larger than that of a similar reaction channel Reaction 124, e.g. the former (producing $O(^1D)$) is around 649 times larger than the latter (producing $O(^3P)$) for a gas temperature of 350 K. Moreover, Reaction 124 with the same rate coefficient is included in the studies containing oxygen chemistry [22, 56, 64, 70, 72, 115], while Reaction 125 is not considered in these studies. It should be emphasized that good agreement between the measured and simulated $O_2(a^1\Delta_g)$ densities is achieved in the work of Dias *et al* [64], and worse agreement can be obtained in the case of considering Reaction 125 with the aforementioned rate coefficient in their simulations due to the significant $O_2(a^1\Delta_g)$ loss. Therefore, Reaction 125 is excluded from the current work.

Table A3. The additionally considered volume reactions in the He/O₂ model compared to our previous work [17]. Reaction 1–4 are additionally considered due to the inclusion of $O_2(b^1\Sigma_{g+})$ in the current chemical model. Reaction 5–16 and 17–87 are additionally considered in this study based on the work of Dias *et al* [64] and Brisset *et al* [72], respectively. ‘O₂’ in this table represents $O_2(X, v = 0)$. The rate coefficient units are given in $\text{m}^3 \text{ s}^{-1}$ and $\text{m}^6 \text{ s}^{-1}$ for two- and three-body reactions, respectively. T_e is in eV, and T_g is in K. The rate coefficient for cases marked with $f(\epsilon)$ is taken from a look-up-table calculated via the referenced cross-section self-consistently coupled to the EEDF [60]. The reverse reaction rate coefficients of the electron-impact excitation labeled with a symbol ‘**’ near the number are calculated via the principle of *detailed balancing* [59]. For the ‘Reaction’ labeled with a symbol ‘~’ near the number, the ‘Rate coefficient’ of the electronically excited state is assumed to be the same as that of the corresponding lower state or that of $O_2(X, v = 0)$.

#	Reaction	Rate coefficient	References
R1–R4 from IST-Lisbon database [62, 63]			
1*	$e + O_2 \rightarrow e + O_2(b^1\Sigma_{g+})$	$f(\epsilon)$	[62, 63]
2*	$e + O_2(a^1\Delta_g) \rightarrow e + O_2(b^1\Sigma_{g+})$	$f(\sigma)$	[62, 63] ^a
3	$e + O_2(b^1\Sigma_{g+}) \rightarrow e + O(^3P) + O(^3P)$	$f(\sigma)$	[62, 63] ^a
4	$e + O_2(b^1\Sigma_{g+}) \rightarrow e + O(^3P) + O(^1D)$	$f(\sigma)$	[62, 63] ^a
R5–R16 from Dias <i>et al</i> [64]			
5	$O_2(a^1\Delta_g) + O_2(a^1\Delta_g) \rightarrow O_2(b^1\Sigma_{g+}) + O_2$	$1.81 \times 10^{-24} (T_g/300)^{3.8} \exp(700/T_g)$	[116]
6	$O_2(b^1\Sigma_{g+}) + O(^3P) \rightarrow O_2(a^1\Delta_g) + O(^3P)$	4×10^{-20}	[117]
7	$O_2(b^1\Sigma_{g+}) + O(^3P) \rightarrow O_2 + O(^3P)$	$4 \times 10^{-20} + 1 \times 10^{-16} \exp(-3700/T_g)$	[117, 118]
8	$O_2(b^1\Sigma_{g+}) + O(^3P) \rightarrow O_2 + O(^1D)$	$3.39 \times 10^{-17} (300/T_g)^{0.1} \exp(-4201/T_g)$	[119]
9	$2O(^3P) + O_2 \rightarrow O_2(b^1\Sigma_{g+}) + O_2$	$0.17 \times 3.81 \times 10^{-42} T_g^{-1} \exp(-170/T_g)$	[99, 108]
10	$O(^1D) + O_2 \rightarrow O(^3P) + O_2(b^1\Sigma_{g+})$	$2.56 \times 10^{-17} \exp(67/T_g)$	[99]
11	$O_2(b^1\Sigma_{g+}) + O_3 \rightarrow 2O_2 + O(^3P)$	1.5×10^{-17}	[99]
12	$O(^3P) + O_3 \rightarrow O_2(b^1\Sigma_{g+}) + O_2$	$0.17 \times 1.8 \times 10^{-17} \exp(-2300/T_g)$	[99, 108]
13	$O^- + O_2(b^1\Sigma_{g+}) \rightarrow O(^3P) + O_2 + e$	6.9×10^{-16}	[99]
14	$O_2(a^1\Delta_g) + O(^3P) + O_2 \rightarrow O_2 + O(^3P) + O_2$	3×10^{-44}	[120]
15	$O(^3P) + O_3 \rightarrow O_2(a^1\Delta_g) + O_2$	$0.33 \times 1.8 \times 10^{-17} \exp(-2300/T_g)$	[99, 108]
16	$O^+ + O_2(a^1\Delta_g) \rightarrow O_2^+ + O(^3P)$	$2 \times 10^{-17} (300/T_g)^{0.5}$	[99, 121]

(Continued.)

Table A3. (Continued.)

#	Reaction	Rate coefficient	References
R17–R87 from Brisset et al [72]			
17	$e + O_3 \rightarrow O(^1D) + O_2(a^1\Delta_g) + e$	$3.22 \times 10^{-13} T_e^{-1.18} \exp(-9.17/T_e)$	[22, 122]
18	$e + O_3^- \rightarrow O_3 + 2e$	$2.12 \times 10^{-14} T_e^{0.51} \exp(-5.87/T_e)$	[22, 123]
19	$e + O_3^- \rightarrow O_2 + O(^3P) + 2e$	$7.12 \times 10^{-14} T_e^{-0.132} \exp(-5.94/T_e)$	[22, 123]
20	$e + O_3^- \rightarrow 3O(^3P) + 2e$	$1.42 \times 10^{-14} T_e^{-0.52} \exp(-9.30/T_e)$	[22, 123]
21	$e + O_2^+ \rightarrow 2O(^1D)$	$5.85 \times 10^{-15} T_e^{-0.7}$	[124]
22	$e + O_4^+ \rightarrow O(^3P) + O(^1D) + O_2$	2.02×10^{-14}	[22, 125, 126]
23~	$He^+ + O_2(b^1\Sigma_g^+) \rightarrow He + O(^3P) + O^+$	$1.07 \times 10^{-15} (300/T_g)^{-0.5}$	[56]
24~	$He^+ + O_2(b^1\Sigma_g^+) \rightarrow He + O_2^+$	$3.3 \times 10^{-17} (300/T_g)^{-0.5}$	[56]
25	$He_2^+ + O(^3P) \rightarrow 2He + O^+$	9×10^{-16}	[22, 127–129]
26	$He_2^+ + O(^1D) \rightarrow 2He + O^+$	9×10^{-16}	[22, 127–129]
27	$He_2^+ + O_2 \rightarrow 2He + O(^3P) + O^+$	1×10^{-16}	[22, 130]
28	$He_2^+ + O_2 \rightarrow 2He + O_2^+$	9×10^{-16}	[22, 130]
29	$He_2^+ + O_2(a^1\Delta_g) \rightarrow 2He + O_2^+$	1.2×10^{-15}	[22, 127–129]
30	$He_2^+ + O_2(b^1\Sigma_g^+) \rightarrow 2He + O_2^+$	1.2×10^{-15}	[22, 127–129]
31	$He_2^+ + O_3 \rightarrow 2He + O^+ + O_2$	1.6×10^{-15}	[22, 127–129]
32	$O_2^+ + He(2^3S) \rightarrow He + O(^3P) + O^+$	8.20×10^{-15}	[22, 127, 128, 131]
33	$O_4^+ + He \rightarrow O_2^+ + O_2 + He$	3.40×10^{-20}	[22, 130]
34	$O_4^+ + He(2^3S) \rightarrow O_2^+ + O_2 + He$	8.00×10^{-15}	[22, 127, 128, 131]
35	$O_4^+ + O(^1D) \rightarrow O(^3P) + O_2 + O_2^+$	3.00×10^{-16}	[22, 127, 128, 132]
36	$O_4^+ + O(^1D) \rightarrow O_3 + O_2^+$	3.00×10^{-16}	[22, 127, 128, 132]
37	$O_4^+ + O_2(a^1\Delta_g) \rightarrow 2O_2 + O_2^+$	6.00×10^{-16}	[22, 127–129]
38	$O_4^+ + O_2(b^1\Sigma_g^+) \rightarrow 2O_2 + O_2^+$	6.00×10^{-16}	[22]
39	$O^- + He \rightarrow e + He + O(^3P)$	$2.50 \times 10^{-24} (T_g/300)^{0.6}$	[21, 22, 133]
40	$O^- + He(2^3S) \rightarrow 2e + He + O^+$	8.70×10^{-15}	[22, 127, 128, 131]
41	$O^- + O(^1D) \rightarrow 2O(^3P) + e$	7.40×10^{-16}	[22, 127, 128, 132]
42	$O^- + O_2 \rightarrow O_2^- + O(^3P)$	1.00×10^{-18}	[22, 130]
43~	$O^- + O_2(b^1\Sigma_g^+) \rightarrow O(^3P) + O_2^-$	1×10^{-16}	[33]
44~	$O^- + O_2(b^1\Sigma_g^+) \rightarrow e + O_3$	$0.75 \times 1.9 \times 10^{-16}$	[99]
45	$O_2^- + He \rightarrow e + He + O_2$	$3.90 \times 10^{-16} \exp(-7400/T_g)$	[22, 134]
46	$O_2^- + He(2^3S) \rightarrow 2e + He + O_2^+$	8.30×10^{-15}	[22, 127, 128, 131]
47~	$O_2^- + O(^1D) \rightarrow e + O_3$	$1.5 \times 10^{-16} (300/T_g)^{-0.5}$	[56]
48~	$O_2^- + O(^1D) \rightarrow O_2 + O^-$	$1.5 \times 10^{-16} (300/T_g)^{-0.5}$	[56]
49	$O_2^- + O_2 \rightarrow O(^3P) + O_3^-$	3.50×10^{-21}	[130]
50~	$O_2^- + O_2(b^1\Sigma_g^+) \rightarrow e + 2O_2$	$2 \times 10^{-16} (300/T_g)^{0.5}$	[56]
51	$O_3^- + He(2^3S) \rightarrow 2e + He + O(^3P) + O_2^+$	8.10×10^{-15}	[22, 127, 128, 131]
52	$O_3^- + O(^1D) \rightarrow O(^3P) + O_2 + O^-$	3.00×10^{-16}	[22, 127–129]
53	$O_3^- + O(^1D) \rightarrow O(^3P) + O_3 + e$	3.00×10^{-16}	[22, 127, 128, 132]
54	$O_3^- + O_2(b^1\Sigma_g^+) \rightarrow O^- + 2O_2$	$6.70 \times 10^{-16} \exp(-1300/T_g)$	[22, 127–129]
55	$O_4^- + He \rightarrow He + O_2 + O_2^-$	$2.20 \times 10^{-11} (T_g/300)^{-1} \exp(-6300/T_g)$	[135]
56	$O_4^- + He(2^3S) \rightarrow 2e + He + O_2 + O_2^+$	8.00×10^{-15}	[22, 127, 128, 131]
57	$O_4^- + O(^1D) \rightarrow e + O(^3P) + 2O_2$	2.00×10^{-16}	[22, 127–129]
58	$O_4^- + O(^1D) \rightarrow O(^3P) + O_2 + O_2^-$	2.00×10^{-16}	[22, 127–129]
59	$O_4^- + O(^1D) \rightarrow 2O_2 + O^-$	2.00×10^{-16}	[22, 127–129]
60	$O_4^- + O_2 \rightarrow 2O_2 + O_2^-$	$2.20 \times 10^{-11} (T_g/300)^{-1} \exp(-6300/T_g)$	[135]
61	$O_4^- + O_2(a^1\Delta_g) \rightarrow 3O_2 + e$	3.00×10^{-16}	[22, 127–129]
62	$O_4^- + O_2(a^1\Delta_g) \rightarrow 2O_2 + O_2^-$	3.00×10^{-16}	[22, 127–129]
63	$O_4^- + O_2(b^1\Sigma_g^+) \rightarrow e + 3O_2$	3.00×10^{-16}	[22, 127–129]
64	$O_4^- + O_2(b^1\Sigma_g^+) \rightarrow 2O_2 + O_2^-$	3.00×10^{-16}	[22, 127–129]
65	$O_4^- + O_3 \rightarrow 2O_2 + O_3^-$	8.00×10^{-16}	[22, 127–129]
66	$He + O_2(b^1\Sigma_g^+) \rightarrow He + O_2(a^1\Delta_g)$	$1.00 \times 10^{-23} (T_g/300)^{0.5}$	estimated value in [56]
67~	$He(2^3S) + O_2(a^1\Delta_g) \rightarrow He + O_2^+ + e$	$2.54 \times 10^{-16} (300/T_g)^{-0.5}$	[56]
68~	$He(2^3S) + O_2(b^1\Sigma_g^+) \rightarrow He + O_2^+ + e$	$2.54 \times 10^{-16} (300/T_g)^{-0.5}$	[56]
69~	$He_2^* + O(^3P) \rightarrow e + 2He + O^+$	3.60×10^{-16}	[104, 105]
70~	$He_2^* + O(^1D) \rightarrow e + 2He + O^+$	3.60×10^{-16}	[104, 105]
71~	$He_2^* + O_2(a^1\Delta_g) \rightarrow e + 2He + O_2^+$	3.60×10^{-16}	[104, 105]
72~	$He_2^* + O_2(b^1\Sigma_g^+) \rightarrow e + 2He + O_2^+$	3.60×10^{-16}	[104, 105]

(Continued.)

Table A3. (Continued.)

73~	$\text{He}_2^* + \text{O}_3 \rightarrow e + 2\text{He} + \text{O}_2^+ + \text{O}(^3\text{P})$	3.60×10^{-16}	[104, 105]
74	$2\text{O}_2 \rightarrow 2\text{O}(^3\text{P}) + \text{O}_2$	$6.60 \times 10^{-15} (T_g/300)^{-1.5} \exp(-59000/T_g)$	[135]
75	$\text{O}_2 + \text{O}_2(b^1\Sigma_{g+}) \rightarrow \text{O}_2 + \text{O}_2(a^1\Delta_g)$	$3.60 \times 10^{-23} (T_g/300)^{0.5}$	[56]
76	$\text{O}_2(a^1\Delta_g) + \text{O}_2(b^1\Sigma_{g+}) \rightarrow \text{O}_2 + \text{O}_2(b^1\Sigma_{g+})$	2.70×10^{-23}	[22]
77	$\text{O}_2(b^1\Sigma_{g+}) + \text{O}_2(b^1\Sigma_{g+}) \rightarrow \text{O}_2 + \text{O}_2(b^1\Sigma_{g+})$	2.70×10^{-23}	[22]
78	$\text{O}_2(b^1\Sigma_{g+}) + \text{O}_3 \rightarrow \text{O}_2 + \text{O}_3$	$5.50 \times 10^{-18} \exp(-135/T_g)$	[22, 136]
79	$\text{O}_2(b^1\Sigma_{g+}) + \text{O}_3 \rightarrow \text{O}_2(a^1\Delta_g) + \text{O}_3$	$5.50 \times 10^{-18} \exp(-135/T_g)$	[22, 136]
80	$\text{He} + \text{He}(2^3\text{S}) + \text{O}(^3\text{P}) \rightarrow e + 2\text{He} + \text{O}^+$	1.60×10^{-43}	[22]
81	$\text{He} + \text{He}(2^3\text{S}) + \text{O}(^1\text{D}) \rightarrow e + 2\text{He} + \text{O}^+$	1.60×10^{-43}	[22]
82	$\text{He} + \text{He}(2^3\text{S}) + \text{O}_2 \rightarrow e + 2\text{He} + \text{O}_2^+$	1.60×10^{-43}	[137]
83	$\text{He} + \text{He}(2^3\text{S}) + \text{O}_2(a^1\Delta_g) \rightarrow e + 2\text{He} + \text{O}_2^+$	1.60×10^{-43}	[22]
84	$\text{He} + \text{He}(2^3\text{S}) + \text{O}_2(b^1\Sigma_{g+}) \rightarrow e + 2\text{He} + \text{O}_2^+$	1.60×10^{-43}	[22]
85	$\text{He} + \text{He}(2^3\text{S}) + \text{O}_3 \rightarrow e + 2\text{He} + \text{O}_2^+ + \text{O}(^3\text{P})$	1.60×10^{-43}	[22]
86	$\text{He} + 2\text{O}(^3\text{P}) \rightarrow \text{He} + \text{O}_2(b^1\Sigma_{g+})$	$2.00 \times 10^{-45} (T_g/300)^{-1} \exp(-170/T_g)$	[22, 138, 139]
87	$\text{He} + \text{O}(^3\text{P}) + \text{O}_2(a^1\Delta_g) \rightarrow \text{He} + \text{O}(^3\text{P}) + \text{O}_2$	4.00×10^{-45}	[120, 140]

^a The rate coefficient for cases marked with $f(\sigma)$ is directly evaluated according to the calculated EEDF and the corresponding electron-impact cross-section from ‘‘Ref’’.

Table A4. The additionally considered electron-impact excitation reactions in the He/O₂ model compared to our previous work [17]. These reactions represent the excitation from ground state to vibrationally excited states and high electronically excited states, which belongs to the helium [61, 62] or oxygen [62, 63] complete set of the IST-Lisbon database yielding good agreement between calculated and measured swarm parameters. Note that these vibrationally excited states and high electronically excited states are not considered as species in our He/O₂ model. In other words, the production and destruction of these states (see equation (1) in [17]) are not considered. Only the energy loss due to these excitation reactions (see equation (11) in [17]) is taken into account based on the corresponding threshold values given in table A4. For the sake of clarity, only the threshold values in the complete set of the IST-Lisbon database [61–63] are presented while the corresponding state notations are omitted. ‘O₂’ in this table represents O₂(X, v = 0). The rate coefficient for cases marked with $f(\epsilon)$ is taken from a look-up-table calculated via the referenced cross-section self-consistently coupled to the EEDF [60].

#	Excitation	Energy threshold (eV)	Rate coefficient	References
1	$e + \text{He} \rightarrow e + \text{He}$	20.62	$f(\epsilon)$	[61, 62]
2	$e + \text{He} \rightarrow e + \text{He}$	20.96	$f(\epsilon)$	[61, 62]
3	$e + \text{He} \rightarrow e + \text{He}$	21.218	$f(\epsilon)$	[61, 62]
4	$e + \text{He} \rightarrow e + \text{He}$	22.719	$f(\epsilon)$	[61, 62]
5	$e + \text{He} \rightarrow e + \text{He}$	22.919	$f(\epsilon)$	[61, 62]
6	$e + \text{He} \rightarrow e + \text{He}$	23.009	$f(\epsilon)$	[61, 62]
7	$e + \text{He} \rightarrow e + \text{He}$	23.069	$f(\epsilon)$	[61, 62]
8	$e + \text{He} \rightarrow e + \text{He}$	23.069	$f(\epsilon)$	[61, 62]
9	$e + \text{He} \rightarrow e + \text{He}$	23.09	$f(\epsilon)$	[61, 62]
10	$e + \text{He} \rightarrow e + \text{He}$	23.589	$f(\epsilon)$	[61, 62]
11	$e + \text{He} \rightarrow e + \text{He}$	23.669	$f(\epsilon)$	[61, 62]
12	$e + \text{He} \rightarrow e + \text{He}$	23.709	$f(\epsilon)$	[61, 62]
13	$e + \text{He} \rightarrow e + \text{He}$	23.739	$f(\epsilon)$	[61, 62]
14	$e + \text{He} \rightarrow e + \text{He}$	23.739	$f(\epsilon)$	[61, 62]
15	$e + \text{He} \rightarrow e + \text{He}$	23.739	$f(\epsilon)$	[61, 62]
16	$e + \text{He} \rightarrow e + \text{He}$	23.739	$f(\epsilon)$	[61, 62]
17	$e + \text{He} \rightarrow e + \text{He}$	23.74	$f(\epsilon)$	[61, 62]
18	$e + \text{He} \rightarrow e + \text{He}$	23.972	$f(\epsilon)$	[61, 62]
19	$e + \text{He} \rightarrow e + \text{He}$	24.011	$f(\epsilon)$	[61, 62]
20	$e + \text{He} \rightarrow e + \text{He}$	24.028	$f(\epsilon)$	[61, 62]
21	$e + \text{He} \rightarrow e + \text{He}$	24.043	$f(\epsilon)$	[61, 62]
22	$e + \text{He} \rightarrow e + \text{He}$	24.043	$f(\epsilon)$	[61, 62]
23	$e + \text{He} \rightarrow e + \text{He}$	24.043	$f(\epsilon)$	[61, 62]
24	$e + \text{He} \rightarrow e + \text{He}$	24.043	$f(\epsilon)$	[61, 62]
25	$e + \text{He} \rightarrow e + \text{He}$	24.046	$f(\epsilon)$	[61, 62]
26	$e + \text{He} \rightarrow e + \text{He}$	24.169	$f(\epsilon)$	[61, 62]
27	$e + \text{He} \rightarrow e + \text{He}$	24.191	$f(\epsilon)$	[61, 62]
28	$e + \text{He} \rightarrow e + \text{He}$	24.201	$f(\epsilon)$	[61, 62]
29	$e + \text{He} \rightarrow e + \text{He}$	24.209	$f(\epsilon)$	[61, 62]
30	$e + \text{He} \rightarrow e + \text{He}$	24.209	$f(\epsilon)$	[61, 62]

(Continued.)

Table A4. (Continued.)

#	Excitation	Energy threshold (eV)	Rate coefficient	References
31	$e + \text{He} \rightarrow e + \text{He}$	24.21	$f(\epsilon)$	[61, 62]
32	$e + \text{He} \rightarrow e + \text{He}$	24.21	$f(\epsilon)$	[61, 62]
33	$e + \text{He} \rightarrow e + \text{He}$	24.211	$f(\epsilon)$	[61, 62]
34	$e + \text{He} \rightarrow e + \text{He}$	24.285	$f(\epsilon)$	[61, 62]
35	$e + \text{He} \rightarrow e + \text{He}$	24.298	$f(\epsilon)$	[61, 62]
36	$e + \text{He} \rightarrow e + \text{He}$	24.304	$f(\epsilon)$	[61, 62]
37	$e + \text{He} \rightarrow e + \text{He}$	24.31	$f(\epsilon)$	[61, 62]
38	$e + \text{He} \rightarrow e + \text{He}$	24.31	$f(\epsilon)$	[61, 62]
39	$e + \text{He} \rightarrow e + \text{He}$	24.31	$f(\epsilon)$	[61, 62]
40	$e + \text{He} \rightarrow e + \text{He}$	24.31	$f(\epsilon)$	[61, 62]
41	$e + \text{He} \rightarrow e + \text{He}$	24.311	$f(\epsilon)$	[61, 62]
42	$e + \text{O}_2 \rightarrow e + \text{O}_2$	4.5	$f(\epsilon)$	[62, 63]
43	$e + \text{O}_2 \rightarrow e + \text{O}_2$	9.97	$f(\epsilon)$	[62, 63]
44	$e + \text{O}_2 \rightarrow e + \text{O}_2$	14.7	$f(\epsilon)$	[62, 63]
45	$e + \text{O}(^3\text{P}) \rightarrow e + \text{O}(^3\text{P})$	4.18	$f(\sigma)$	[62, 63] ^a
46	$e + \text{O}(^3\text{P}) \rightarrow e + \text{O}(^3\text{P})$	9.2	$f(\sigma)$	[62, 63] ^a
47	$e + \text{O}(^3\text{P}) \rightarrow e + \text{O}(^3\text{P})$	12.5	$f(\sigma)$	[62, 63] ^a
48	$e + \text{O}(^3\text{P}) \rightarrow e + \text{O}(^3\text{P})$	14.1	$f(\sigma)$	[62, 63] ^a
49	$e + \text{O}(^3\text{P}) \rightarrow e + \text{O}(^3\text{P})$	15.7	$f(\sigma)$	[62, 63] ^a
50	$e + \text{O}_2 \rightarrow e + \text{O}_2$	0.19	$f(\epsilon)$	[62, 63]
51	$e + \text{O}_2 \rightarrow e + \text{O}_2$	0.38	$f(\epsilon)$	[62, 63]
52	$e + \text{O}_2 \rightarrow e + \text{O}_2$	0.6	$f(\epsilon)$	[62, 63]
53	$e + \text{O}_2 \rightarrow e + \text{O}_2$	0.8	$f(\epsilon)$	[62, 63]

^a The rate coefficient for cases marked with $f(\sigma)$ is directly evaluated according to the calculated EEDF and the corresponding electron-impact cross-section from ‘‘Ref’’.

Table A5. The electron-impact elastic collisions in the He/O₂ model. For updates compared to our previous work [17] see notes below the table. ‘O₂’ in this table represents O₂(X, v = 0).

#	Collision	References
1	$e + \text{He} \rightarrow e + \text{He}$	[61, 62]
4	$e + \text{O}(^3\text{P}) \rightarrow e + \text{O}(^3\text{P})$	[62, 63]
5 ^a	$e + \text{O}_2 \rightarrow e + \text{O}_2$	[62, 63]

^a Compared to our previous work [17], the ‘Ref’ is updated. Specifically, the cross-section data of reaction 5 in ‘Ref’ [62, 63] are used in the current work instead of those in ‘Ref’ [17].

Note: The ‘Reaction’ containing nitrogen species in [17] (i.e. reactions 2–3 and 7–9) are deleted.

Note: The ‘Reaction’ (i.e. reaction 6) is deleted due to an improved treatment of the elastic collision cross-section data.

Table A6. The neutral wall reactions in the He/O₂ model. For updates compared to our previous work [17] see notes below the table. ‘O₂’ in this table represents O₂(X, v = 0).

#	Reaction	Probability(γ)	References
1	$\text{He}(2^3\text{S}) + \text{wall} \rightarrow \text{He}$	1	[19, 141]
2	$\text{He}_2^* + \text{wall} \rightarrow 2\text{He}$	1	[19, 141]
7	$\text{O}(^1\text{D}) + \text{wall} \rightarrow \text{O}(^3\text{P})$	1	[106] ^a
8	$\text{O}_2(a^1\Delta_g) + \text{wall} \rightarrow \text{O}_2$	0.00022	[65] ^a
14	$\text{O}(^3\text{P}) + \text{wall} \rightarrow 1/2\text{O}_2$	0.002	estimated from [65] ^b
15	$\text{O}_2(b^1\Sigma_{g+}) + \text{wall} \rightarrow \text{O}_2$	0.135	[118] ^b

^a Compared to our previous work [17], the probabilities of reactions 7 and 8 are updated in this study to be consistent with those of Dias *et al* [64].

^b Reactions 14 and 15 are additionally considered in this study based on the work of Dias *et al* [64]. The probabilities of reaction 14 as a function of pressure, discharge current and wall temperature reported in [64] are estimated to a constant value in this study. This constant is around the most frequent value of the probabilities reported in [64], see section 4.

Note: The ‘Reaction’ containing nitrogen species in [17] (i.e. reactions 3–6 and 11) are deleted.

Note: The ‘Reaction’ which is included for a test of the sensitivity analysis in [17] (i.e. reactions 9, 10 and 13) are deleted.

Note: The ‘Reaction’ containing O₂(X, v > 0) (i.e. reaction 12) is deleted due to the exclusion of vibrationally excited molecules from the current work.

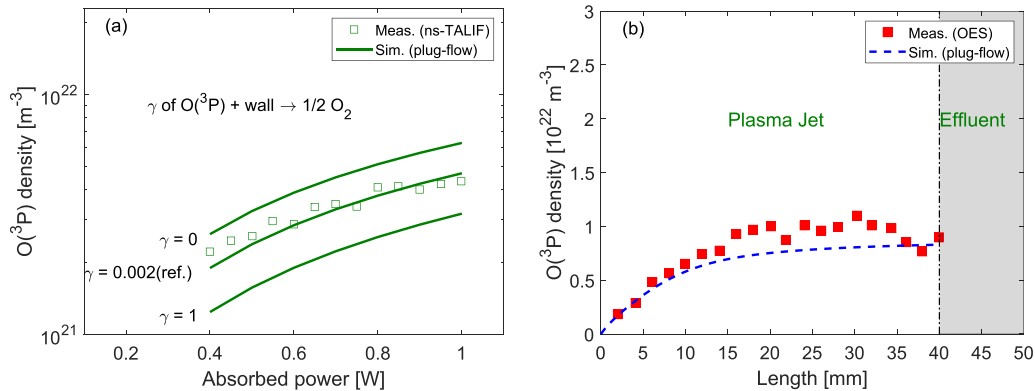


Figure B1. (a) The atomic oxygen density at the middle of the plasma channel measured with the ns-TALIF method in a He/O₂ μ APPJ by Waskoenig *et al* [33] (\square) together with the plug-flow model calculation results at the middle of the plasma channel in this work calculated with the neutral wall reaction probability $\gamma = 0.002$ (the reference value) and other different γ values of $O(^3P) + \text{wall} \rightarrow 1/2 O_2$ (—) for a variation of the absorbed power from 0.40 W to 1.00 W. (b) The spatially resolved atomic oxygen density measured with the OES method (assisted by numerical simulation) in the gas flow direction of a He/O₂ μ APPJ by Bibinov *et al* [34] (\blacksquare) and the corresponding plug-flow model calculation results in this work (---). More details regarding the μ APPJs such as the operating conditions and the measurement methods, see section 2.

Appendix B. Comparison between the simulation results in this work and the measurement data of the He/O₂ μ APPJs considered in previous work [17]

The measurement data of the He/O₂ μ APPJs by Waskoenig *et al* [33] and Bibinov *et al* [34] considered in previous work [17] and the corresponding simulated atomic oxygen densities in this work using the plug-flow model in section 3 and the chemical kinetics in section 4 are presented in figure B1. The sensitivity of the simulated atomic oxygen density to the neutral wall reaction probability γ of $O(^3P) + \text{wall} \rightarrow 1/2 O_2$ is shown in figure B1(a), and compared with measurement data from Waskoenig *et al* [33]. For instance at 1 W, as γ is modified from 0 to 1, the simulated atomic oxygen density is modified from $6.3 \times 10^{21} m^{-3}$ to $3.2 \times 10^{21} m^{-3}$. The modification is particularly significant as γ is modified from 1×10^{-4} to 5×10^{-2} , where the atomic oxygen density is modified from $6.1 \times 10^{21} m^{-3}$ to $3.3 \times 10^{21} m^{-3}$ (not shown here). This is equivalent to around 90% of the total variation as γ is modified from 0 to 1 ($(6.1 - 3.3)/(6.3 - 3.2) = 90\%$). The reference value of 0.002 used in this work locates in this sensitive range. Similar percentage values and conclusions are obtained for other absorbed powers. In figures B1(a) and (b), a good agreement between the measurement data and the simulation results is similarly obtained in this work relative to those comparisons in previous work [17]. However, due to the assumption of the 5% power transfer efficiency used in the simulations of the aforementioned μ APPJs [33, 34] (not used in section 5), these calculation results in figure B1 are only used as a comparison with those in previous study [17], and are only considered in appendix B, see section 2. Note that these results are not analyzed in section 5, since the 5% power transfer efficiency used in [33, 34] could lead to the potential inconsistencies between the input parameters of measurements and simulations.

ORCID iDs

Youfan He 0000-0003-1275-7695

Ralf Peter Brinkmann 0000-0002-2581-9894

Efe Kemaneci 0000-0002-5540-0947

Andrew R Gibson 0000-0002-1082-4359

References

- [1] Winter J, Brandenburg R and Weltmann K-D 2015 Atmospheric pressure plasma jets: an overview of devices and new directions *Plasma Sources Sci. Technol.* **24** 064001
- [2] Penkov O V, Khadem M, Lim W-S and Kim D-E 2015 A review of recent applications of atmospheric pressure plasma jets for materials processing *J. Coat. Technol. Res.* **12** 225–35
- [3] Fanelli F and Fracassi F 2017 Atmospheric pressure non-equilibrium plasma jet technology: general features, specificities and applications in surface processing of materials *Surf. Coat. Technol.* **322** 174–201
- [4] Reuter S, von Woedtke T and Weltmann K-D 2018 The kinpen-a review on physics and chemistry of the atmospheric pressure plasma jet and its applications *J. Appl. Phys.* **51** 233001
- [5] Lu X, Liu D, Xian Y, Nie L, Cao Y and He G 2021 Cold atmospheric-pressure air plasma jet: physics and opportunities *Phys. Plasmas* **28** 100501
- [6] Viegas P, Slikboer E, Bonaventura Z, Guaitella O, Sobota A and Bourdon A 2022 Physics of plasma jets and interaction with surfaces: review on modelling and experiments *Plasma Sources Sci. Technol.* **31** 053001
- [7] Urbanietz T, Böke M, Schulz von der Gathen V and von Keudell A 2018 Non-equilibrium excitation of CO₂ in an atmospheric pressure helium plasma jet *J. Appl. Phys.* **51** 345202
- [8] Stewig C, Schüttler S, Urbanietz T, Böke M and von Keudell A 2020 Excitation and dissociation of CO₂

- heavily diluted in noble gas atmospheric pressure plasma *J. Appl. Phys.* **53** 125205
- [9] Du Y, Tsankov T V, Luggenhölscher D and Czarnetzki U 2021 Time evolution of CO₂ ro-vibrational excitation in a nanosecond discharge measured with laser absorption spectroscopy *J. Appl. Phys.* **54** 365201
- [10] Du Y, Tsankov T V, Luggenhölscher D and Czarnetzki U 2021 Nanosecond resolved ro-vibrational CO₂ excitation measurement *J. Appl. Phys.* **54** 34LT02
- [11] Vervloedt S C L and von Keudell A 2024 Ammonia synthesis by plasma catalysis in an atmospheric RF helium plasma *Plasma Sources Sci. Technol.* **33** 045005
- [12] Yu S, Vervloedt S C L and von Keudell A 2024 Controlled synthesis of NO in an atmospheric pressure plasma by suppressing NO destruction channels by plasma catalysis *J. Appl. Phys.* **57** 245203
- [13] Kim C-H, Kwon S, Bahn J H, Lee K, Jun S I, Rack P D and Baek S J 2010 Effects of atmospheric nonthermal plasma on invasion of colorectal cancer cells *Appl. Phys. Lett.* **96** 243701
- [14] Fricke K, Reuter S, Schroder D, Schulz-von der Gathen V, Weltmann K-D and von Woedtke T 2012 Investigation of surface etching of poly(ether ether ketone) by atmospheric-pressure plasmas *IEEE Trans. Plasma Sci.* **40** 2900–11
- [15] West A 2016 Optical and electrical diagnosis of atmospheric pressure plasma jets *PhD Thesis* University of York
- [16] West A, van der Schans M, Xu C, Cooke M and Wagenaars E 2016 Fast, downstream removal of photoresist using reactive oxygen species from the effluent of an atmospheric pressure plasma jet *Plasma Sources Sci. Technol.* **25** 02LT01
- [17] He Y et al 2021 Zero-dimensional and pseudo-one-dimensional models of atmospheric-pressure plasma jets in binary and ternary mixtures of oxygen and nitrogen with helium background *Plasma Sources Sci. Technol.* **30** 105017
- [18] Graves D B 2012 The emerging role of reactive oxygen and nitrogen species in redox biology and some implications for plasma applications to medicine and biology *J. Appl. Phys.* **45** 263001
- [19] Liu D X, Bruggeman P, Iza F, Rong M Z and Kong M G 2010 Global model of low-temperature atmospheric-pressure He + H₂O plasmas *Plasma Sources Sci. Technol.* **19** 025018
- [20] Schröter S et al 2018 Chemical kinetics in an atmospheric pressure helium plasma containing humidity *Phys. Chem. Chem. Phys.* **20** 24263–86
- [21] Liu D-X, Rong M-Z, Wang X-H, Iza F, Kong M G and Bruggeman P 2010 Main species and physicochemical processes in cold atmospheric-pressure He + O₂ plasmas *Plasma Process. Poly.* **7** 846–65
- [22] Turner M M 2015 Uncertainty and error in complex plasma chemistry models *Plasma Sources Sci. Technol.* **24** 035027
- [23] Murakami T, Niemi K, Gans T, O'Connell D and Graham W G 2012 Chemical kinetics and reactive species in atmospheric pressure helium-oxygen plasmas with humid-air impurities *Plasma Sources Sci. Technol.* **22** 015003
- [24] Murakami T, Niemi K, Gans T, O'Connell D and Graham W G 2013 Interacting kinetics of neutral and ionic species in an atmospheric-pressure helium-oxygen plasma with humid air impurities *Plasma Sources Sci. Technol.* **22** 045010
- [25] Murakami T, Niemi K, Gans T, O'Connell D and Graham W G 2014 Afterglow chemistry of atmospheric-pressure helium-oxygen plasmas with humid air impurity *Plasma Sources Sci. Technol.* **23** 025005
- [26] Sun B, Liu D, Iza F, Wang S, Yang A, Liu Z, Rong M and Wang X 2019 Global model of an atmospheric-pressure capacitive discharge in helium with air impurities from 100 to 10 000 ppm *Plasma Sources Sci. Technol.* **28** 035006
- [27] Van Gaens W and Bogaerts A 2013 Kinetic modelling for an atmospheric pressure argon plasma jet in humid air *J. Appl. Phys.* **46** 275201
- [28] Van Gaens W and Bogaerts A 2014 Reaction pathways of biomedically active species in an Ar plasma jet *Plasma Sources Sci. Technol.* **23** 035015
- [29] Van Gaens W, Bruggeman P J and Bogaerts A 2014 Numerical analysis of the NO and O generation mechanism in a needle-type plasma jet *New J. Phys.* **16** 063054
- [30] Vass M'e, Schulenberg D, Donkó Z, Korolov I, Hartmann P, Schulze J and Mussenbrock T 2024 A new 2D fluid-MC hybrid approach for simulating nonequilibrium atmospheric pressure plasmas: density distribution of atomic oxygen in radio-frequency plasma jets in He/O₂ mixtures *Plasma Sources Sci. Technol.* **33** 015012
- [31] Schmidt-Bleker A, Winter J, Bösel A, Reuter S and Weltmann K-D 2015 On the plasma chemistry of a cold atmospheric argon plasma jet with shielding gas device *Plasma Sources Sci. Technol.* **25** 015005
- [32] Golda J et al 2016 Concepts and characteristics of the 'COST Reference Microplasma Jet *J. Appl. Phys.* **49** 084003
- [33] Waskoenig J, Niemi K, Knake N, Graham L M, Reuter S, Schulz von der Gathen V and Gans T 2010 Atomic oxygen formation in a radio-frequency driven micro-atmospheric pressure plasma jet *Plasma Sources Sci. Technol.* **19** 045018
- [34] Bibinov N, Knake N, Bahre H, Awakowicz P and Schulz von der Gathen V 2011 Spectroscopic characterization of an atmospheric pressure μ -jet plasma source *J. Appl. Phys.* **44** 345204
- [35] Riedel F, Golda J, Held J, Davies H L, van der Woude M W, Bredin J, Niemi K, Gans T, Schulz von der Gathen V and O'Connell D 2020 Reproducibility of 'cost reference microplasma jets *Plasma Sources Sci. Technol.* **29** 095018
- [36] Myers B, Barnat E and Stapelmann K 2021 Atomic oxygen density determination in the effluent of the COST reference source using in situ effective lifetime measurements in the presence of a liquid interface *J. Appl. Phys.* **54** 455202
- [37] Steuer D, Korolov I, Chur S, Schulze J, Schulz von der Gathen V, Golda J and Böke M 2021 2D spatially resolved O atom density profiles in an atmospheric pressure plasma jet: from the active plasma volume to the effluent *J. Appl. Phys.* **54** 355204
- [38] Steuer D, van Impel H, Gibson A R, Schulz von der Gathen V, Böke M and Golda J 2022 State enhanced actinometry in the COST microplasma jet *Plasma Sources Sci. Technol.* **31** 10LT01
- [39] Winzer T, Steuer D, Schüttler S, Blosczyk N, Benedikt J and Golda J 2022 RF-driven atmospheric-pressure capillary plasma jet in a He/O₂ gas mixture: multi-diagnostic approach to energy transport *J. Appl. Phys.* **132** 183301
- [40] Turner M M 2015 Uncertainty and sensitivity analysis in complex plasma chemistry models *Plasma Sources Sci. Technol.* **25** 015003
- [41] Berthelot A and Bogaerts A 2017 Modeling of CO₂ plasma: effect of uncertainties in the plasma chemistry *Plasma Sources Sci. Technol.* **26** 115002
- [42] Wang W, Berthelot A, Zhang Q and Bogaerts A 2018 Modelling of plasma-based dry reforming: how do uncertainties in the input data affect the calculation results? *J. Appl. Phys.* **51** 204003

- [43] Tennyson J et al 2022 The 2021 release of the quantum database (QDB) of plasma chemistries and reactions *Plasma Sources Sci. Technol.* **31** 095020
- [44] Hanicinec M, Mohr S and Tennyson J 2020 Fast species ranking for iterative species-oriented skeletal reduction of chemistry sets *Plasma Sources Sci. Technol.* **29** 125024
- [45] Hanicinec M, Mohr S and Tennyson J 2023 A regression model for plasma reaction kinetics *J. Appl. Phys.* **56** 374001
- [46] Vishwakarma G, Sonpal A and Hachmann J 2021 Metrics for benchmarking and uncertainty quantification: quality, applicability and best practices for machine learning in chemistry *Trends Chem.* **3** 146–56
- [47] Willems G, Golda J, Ellerweg D, Benedikt J, von Keudell A, Knake N and Schulz von der Gathen V 2019 Corrigendum: characterization of the effluent of a He/O₂ micro-scaled atmospheric pressure plasma jet by quantitative molecular beam mass spectrometry (2010 *New J. Phys.* 12 013021) *New J. Phys.* **21** 059501
- [48] Korolov I, Steuer D, Bischoff L, Hübner G, Liu Y, Schulz von der Gathen V, Böke M, Mussenbrock T and Schulze J 2021 Atomic oxygen generation in atmospheric pressure RF plasma jets driven by tailored voltage waveforms in mixtures of He and O₂ *J. Appl. Phys.* **54** 125203
- [49] Greb A, Niemi K, O'Connell D and Gans T 2014 Energy resolved actinometry for simultaneous measurement of atomic oxygen densities and local mean electron energies in radio-frequency driven plasmas *Appl. Phys. Lett.* **105** 234105
- [50] Tsutsumi T, Greb A, Gibson A R, Hori M, O'Connell D and Gans T 2017 Investigation of the radially resolved oxygen dissociation degree and local mean electron energy in oxygen plasmas in contact with different surface materials *J. Appl. Phys.* **121** 143301
- [51] Goehlich A, Kawetzi T and Döbele H F 1998 On absolute calibration with xenon of laser diagnostic methods based on two-photon absorption *J. Chem. Phys.* **108** 9362–70
- [52] Niemi K, Schulz von der Gathen V and Döbele H F 2001 Absolute calibration of atomic density measurements by laser-induced fluorescence spectroscopy with two-photon excitation *J. Appl. Phys.* **34** 2330
- [53] Niemi K, Schulz-von der Gathen V and Döbele H F 2005 Absolute atomic oxygen density measurements by two-photon absorption laser-induced fluorescence spectroscopy in an RF-excited atmospheric pressure plasma jet *Plasma Sources Sci. Technol.* **14** 375
- [54] Drag C, Marmuse F and Blondel C 2021 Measurement of the two-photon excitation cross-section of the 6p[3/2]2 and 6p[1/2]0 levels of Xe I at the wavelengths 224.3 and 222.6 nm *Plasma Sources Sci. Technol.* **30** 075026
- [55] Shu Z, Popov N A and Starikovskaia S M 2024 Absolute calibration of the ratio of Xe/O two-photon absorption cross-sections for O-TALIF applications *Plasma Sources Sci. Technol.* **33** 025019
- [56] Stafford D S and Kushner M J 2004 O₂(a¹Δ_g) production in He/O₂ mixtures in flowing low pressure plasmas *J. Appl. Phys.* **96** 2451
- [57] He Y, Kuhfeld J, Lepikhin N D, Czarnetzki U, Guerra V, Brinkmann R P, Gibson A R and Kemaneci E 2024 Zero-dimensional simulations of DC ns-pulsed plasma jet in N₂ at near atmospheric pressure: validation of the vibrational kinetics *Plasma Sources Sci. Technol.* **33** 115011
- [58] Godyak V A, Piejak R B and Alexandrovich B M 1993 Probe diagnostics of non-maxwellian plasmas *J. Appl. Phys.* **73** 3657–63
- [59] Lieberman M A and Lichtenberg A J 2005 *Principles of Plasma Discharges and Materials Processing* (Wiley)
- [60] Tejero del Caz A, Guerra V, Gonçalves D, Lino da Silva M, Marques L, Pinhao N, Pintassilgo C D and Alves L L 2019 The LibOn KInetics boltzmann solver *Plasma Sources Sci. Technol.* **28** 043001
- [61] IST-Lisbon database (available at: www.lxcat.net) (Accessed 27 February 2023)
- [62] Alves L L 2014 The ist-lisbon database on lxcat *J. Phys.: Conf. Ser.* **565** 012007
- [63] IST-Lisbon database (available at: www.lxcat.net) (Accessed 31 October 2023)
- [64] Dias T C, Fromentin C, Alves L L, Tejero del Caz A, Silva T and Guerra V 2023 A reaction mechanism for oxygen plasmas *Plasma Sources Sci. Technol.* **32** 084003
- [65] Booth J-P et al 2020 Determination of absolute O(3P) and O₂(a¹Δ_g) densities and kinetics in fully modulated O₂ dc glow discharges from the O₂(x3Σ_g⁻) afterglow recovery dynamics *Plasma Sources Sci. Technol.* **29** 115009
- [66] Paul D, Mozetic M, Zaplotnik R, Primc G, Donlagić D and Vesel A 2023 A review of recombination coefficients of neutral oxygen atoms for various materials *Materials* **16** 1774
- [67] Chantry P J 1987 A simple formula for diffusion calculations involving wall reflection and low density *J. Appl. Phys.* **62** 1141
- [68] Booth J P and Sadeghi N 1991 Oxygen and fluorine atom kinetics in electron cyclotron resonance plasmas by time-resolved actinometry *J. Appl. Phys.* **70** 611–20
- [69] Gudmundsson J T and Thorsteinsson E G 2007 Oxygen discharges diluted with argon: dissociation processes *Plasma Sources Sci. Technol.* **16** 399
- [70] Guerra V, Tejero del Caz A, Pintassilgo C D and Alves L L 2019 Modelling N₂-O₂ plasmas: volume and surface kinetics *Plasma Sources Sci. Technol.* **28** 073001
- [71] Viegas P, Silveira J, Dias T C, Guaitella O, Sofía Morillo Candás A and Guerra V 2024 Surface recombination in Pyrex in oxygen DC glow discharges: mesoscopic modelling and comparison with experiments *Plasma Sources Sci. Technol.* **33** 055003
- [72] Brisset A, Gibson A R, Schröter S, Niemi K, Booth J-P, Gans T, O'Connell D and Wagenaars E 2021 Chemical kinetics and density measurements of OH in an atmospheric pressure He + O₂ + H₂O radiofrequency plasma *J. Appl. Phys.* **54** 285201
- [73] Research Data Repository of Ruhr University Bochum 2024 2D spatially resolved O atom density profiles in an atmospheric pressure plasma jet: from the active plasma volume to the effluent (available at: rdpcidat.rub.de/node/323)
- [74] Hodge V and Austin J 2004 A survey of outlier detection methodologies *Artif. Intell. Rev.* **22** 85–126
- [75] Wang H, Bah M J and Hammad M 2019 Progress in outlier detection techniques: a survey *IEEE Access* **7** 107964–8000
- [76] Smiti A 2020 A critical overview of outlier detection methods *Comput. Sci. Rev.* **38** 100306
- [77] Nazmul Kabir Sikder Md and Batarseh F A 2023 7-outlier detection using AI: a survey *AI Assurance* ed F A Batarseh and L J Freeman (Academic) pp 231–91
- [78] Bechtold B 2016 Violin Plots for Matlab *GitHub Project* (available at: <https://github.com/bastibe/Violinplot-Matlab>)
- [79] TRINITI database 2019 (available at: www.lxcat.net)
- [80] Deloche R, Monchicourt P, Cheret M and Lambert F 1976 High-pressure helium afterglow at room temperature *Phys. Rev. A* **13** 1140–76
- [81] Flannery M R, McCann K J and Winter N W 1981 Cross sections for electron impact ionisation of metastable rare-gas excimers (He2*, Kr2*, Xe2*) *J. Phys. B: At. Mol. Phys.* **14** 3789

- [82] Bekefi G 1966 *Radiation Processes in Plasmas* (Wiley)
- [83] Lieberman M A 2015 Analytical model of atmospheric pressure, helium/trace gas radio-frequency capacitive Penning discharges *Plasma Sources Sci. Technol.* **24** 025009
- [84] Stalder K R, Vidmar R J, Nersisyan G and Graham W G 2006 Modeling the chemical kinetics of high-pressure glow discharges in mixtures of helium with real air *J. Appl. Phys.* **99** 093301
- [85] Sakiyama Y and Graves D B 2006 Corona-glow transition in the atmospheric pressure RF-excited plasma needle *J. Appl. Phys.* **39** 3644
- [86] Brok W J M, Bowden M D, Van Dijk J, Van der Mullen J J A M and Kroesen G M W 2005 Numerical description of discharge characteristics of the plasma needle *J. Appl. Phys.* **98** 013302
- [87] Golubovskii Y B, Maiorov V A, Behnke J and Behnke J F 2002 Modelling of the homogeneous barrier discharge in helium at atmospheric pressure *J. Appl. Phys.* **36** 39
- [88] Wang Q, Economou D J and Donnelly V M 2006 Simulation of a direct current microplasma discharge in helium at atmospheric pressure *J. Appl. Phys.* **100** 023301
- [89] Alves L L, Gousset G and Ferreira C M 1992 A collisional-radiative model for microwave discharges in helium at low and intermediate pressures *J. Appl. Phys.* **25** 1713
- [90] Capitelli M, Ferreira C M, Gordiets B F and Osipov A I 2001 Book review: Plasma kinetics in atmospheric gases *Plasma Phys. Control. Fusion* **43** 371–2
- [91] Biagi database 2019 (available at: www.lxcat.net)
- [92] Sakiyama Y, Graves D B, Chang H-W, Shimizu T and Morfill G E 2012 Plasma chemistry model of surface microdischarge in humid air and dynamics of reactive neutral species *J. Appl. Phys.* **45** 425201
- [93] Chanin L M, Phelps A V and Biondi M A 1962 Measurements of the attachment of low-energy electrons to oxygen molecules *Phys. Rev.* **128** 219
- [94] Morgan database 2019 (available at: www.lxcat.net)
- [95] Tayal S S and Zatsarinny O 2016 B-spline R-matrix-with-pseudostates approach for excitation and ionization of atomic oxygen by electron collisions *Phys. Rev. A* **94** 042707
- [96] Kossyi I A, Kostinsky A Y, Matveyev A A and Silakov V P 1992 Kinetic scheme of the non-equilibrium discharge in nitrogen-oxygen mixtures *Plasma Sources Sci. Technol.* **1** 207
- [97] Gudmundsson J T and Lieberman M A 2004 Recombination rate coefficients in oxygen discharges *Technical Report* RH-17-2004 (Science Institute, University of Iceland)
- [98] Petrigiani A, Hellberg F, Thomas R D, Larsson M, Cosby P C and van der Zande W J 2005 Vibrational dependence in the dissociative recombination of O_2^+ *J. Phys.: Conf. Ser.* **4** 182
- [99] Eliasson B and Kogelschatz U 1986 Basic data for modeling of electrical discharges in gases: oxygen *Technical Report* (ABB Asea Brown Boveri)
- [100] Böhringer H, Arnold F, Smith D and Adams N G 1983 A study of the temperature dependences of the $N_2^+ + N_2 \rightarrow N_4^+$ and $O_2^+ + O_2 \rightarrow O_4^+$ association reactions using the selected-ion flow-tube and drift-tube techniques *Int. J. Mass Spectrom. Ion Phys.* **52** 25–41
- [101] Fridman A 2008 *Plasma Chemistry* (Cambridge University Press)
- [102] Cenian A, Chernukho A and Borodin V 1995 Modeling of plasma-chemical reactions in gas mixture of CO_2 lasers. II. Theoretical model and its verification *Contrib. Plasma Phys.* **35** 273–96
- [103] Olson R E, Peterson J R and Moseley J 1970 Ion-ion recombination total cross sections-atomic species *J. Chem. Phys.* **53** 3391
- [104] Nayak G, Sadeghi N and Bruggeman P J 2019 He(2^3S_1) and He $_2(a^3\Sigma_u^+)$ metastables densities measured in an RF-driven helium plasma using broadband absorption spectroscopy *Plasma Sources Sci. Technol.* **28** 125006
- [105] Pouvesle J M, Stevefelt J, Lee F W, Jahani H R, Gyls V T and Collins C B 1985 Reactivity of metastable helium molecules in atmospheric pressure afterglows *J. Chem. Phys.* **83** 2836–9
- [106] Gordiets B F, Ferreira C M, Guerra V L, Loureiro J M A H, Nahorny J, Pagnon D, Touzeau M and Vialle M 1995 Kinetic model of a low-pressure N_2 - O_2 flowing glow discharge *IEEE Trans. Plasma Sci.* **23** 750–68
- [107] Lopaev D V, Malykhin E M and Zyryanov S M 2010 Surface recombination of oxygen atoms in O_2 plasma at increased pressure: II. Vibrational temperature and surface production of ozone *J. Appl. Phys.* **44** 015202
- [108] Feoktistov V A, Mukhovatova A V, Popov A M and Rakhimova T V 1995 Self-consistent modelling of low-pressure RF discharges in oxygen plasma *J. Appl. Phys.* **28** 1346
- [109] Belmonte T, Czerwiec T, Gavillet J and Michel H 1997 Synthesis of zirconia thin films by RPECVD: modeling of Ar- O_2 post-discharge and comparison between Ar- O_2 and Ar- O_2 - H_2 post-discharges processes *Surf. Coat. Technol.* **97** 642–8
- [110] Jeong J Y, Park J, Henins I, Babayan S E, Tu V J, Selwyn G S, Ding G and Hicks R F 2000 Reaction chemistry in the afterglow of an oxygen-helium, atmospheric-pressure plasma *J. Phys. Chem.* **104** 8027
- [111] Niles F E 1974 Survey of two-body and three-body reaction-rate coefficients for the ionized stratosphere and mesosphere *Technical Report* (Army Ballistic Research Lab)
- [112] Atkinson R, Baulch D L, Cox R A, Crowley J N, Hampson R F, Hynes R G, Jenkin M E, Rossi M J and Troe J 2004 Evaluated kinetic and photochemical data for atmospheric chemistry: volume I—gas phase reactions of O_x , HO_x , NO_x and SO_x species *Atmos. Chem. Phys.* **4** 1461–738
- [113] National Institute of Standards and Technology 2011 NIST Chemical Kinetics Database (available at: <http://kinetics.nist.gov/>)
- [114] Guerra V and Loureiro J 1999 Kinetic model of a low-pressure microwave discharge in O_2 - H_2 including the effects of O^- ions on the characteristics for plasma maintenance *Plasma Sources Sci. Technol.* **8** 110
- [115] Liu Y, Korolov I, Trieschmann J, Steuer D, Schulz von der Gathen V, Böke M, Bischoff L, Hübner G, Schulze J and Mussenbrock T 2021 Micro atmospheric pressure plasma jets excited in He/ O_2 by voltage waveform tailoring: a study based on a numerical hybrid model and experiments *Plasma Sources Sci. Technol.* **30** 064001
- [116] Heidner R F, Gardner C E, El-Sayed T M, Segal G I and Kasper J V V 1981 Temperature dependence of $O_2(1\Delta)+O_2(1\Delta)$ and $I(2P_{1/2})+O_2(1\Delta)$ energy pooling *J. Chem. Phys.* **74** 5618–26
- [117] Ionin A A, Kochetov I V, Napartovich A P and Yuryshv. N N 2007 Physics and engineering of singlet delta oxygen production in low-temperature plasma *J. Appl. Phys.* **40** R25
- [118] Booth J P et al 2022 Quenching of $O_2(b^1\Sigma_g^-)$ by $O(3P)$ atoms. Effect of gas temperature *Plasma Sources Sci. Technol.* **31** 065012
- [119] Zinn J, Sutherland C D, Stone S N, Duncan L M and Behnke R 1982 Ionospheric effects of rocket exhaust products-heao-c, skylab *J. Atmos. Terr. Phys.* **44** 1143–71

- [120] Braginskiy O V, Vasilieva A N, Klopovskiy K S, Kovalev A S, Lopaev D V, Proshina O V, Rakhimova T V and Rakhimov A T 2005 Singlet oxygen generation in O₂ flow excited by RF discharge: I. homogeneous discharge mode: α -mode *J. Appl. Phys.* **38** 3609
- [121] Annušová A, Marinov D, Booth J-P, Sirse N, Lino da Silva M, Lopez B and Guerra V 2018 Kinetics of highly vibrationally excited O₂(X) molecules in inductively-coupled oxygen plasmas *Plasma Sources Sci. Technol.* **27** 045006
- [122] Gupta M and Baluja K L 2005 Electron collisions with an ozone molecule using the R-matrix method *J. Phys. B: At. Mol. Opt. Phys.* **38** 4057
- [123] Seiersen K, Bak J, Bluhme H, Jensen M J, Nielsen S B and Andersen L H 2003 Electron-impact detachment of O₃⁻, NO₃⁻ and SO₂⁻ ions *Phys. Chem. Chem. Phys.* **5** 4814–20
- [124] Peverall R et al 2001 Dissociative recombination and excitation of O₂⁺: Cross sections, product yields and implications for studies of ionospheric airglows *J. Chem. Phys.* **114** 6679–89
- [125] Florescu-Mitchell A I and Mitchell J B A 2006 Dissociative recombination *Phys. Rep.* **430** 277–374
- [126] Dulaney J L, Biondi M A and Johnsen R 1988 Electron-temperature dependence of the recombination of electrons with O₄⁺ ions *Phys. Rev. A* **37** 2539–42
- [127] Eichelberger B R, Snow T P and Bierbaum V M 2003 Collision rate constants for polarizable ions *J. Am. Soc. Mass Spectrom.* **14** 501–5
- [128] Langevin M P 1905 Une formule fondamentale de théorie cinétique *Ann. Chim. Phys.* **5** 245–88
- [129] Miller T M 2000 *Atomic and Molecular Polarizabilities (Handbook of Chemistry and Physics vol 77)* (CRC Press) pp 193–202
- [130] Ikezoe Y 1987 *Gas Phase Ion-molecule Reaction Rate Constants through 1986* (Ion Reaction Research Group of the Mass Spectroscopy Society of Japan) (available at: www.mssj.jp/english/publications/books.html)
- [131] Crosby D A and Zorn J C 1977 Dipole polarizability of 2³s₁ and 2¹s₀ metastable helium measured by the electric deflection time-of-flight method *Phys. Rev. A* **16** 488–91
- [132] Nesbet R K 1977 Atomic polarizabilities for ground and excited states of C, N and O *Phys. Rev. A* **16** 1–5
- [133] Penent F, Grouard J P, Hall R I, Montmagnon J L, Champion R L, Doverspike L D and Esaulov V A 1987 Fundamental processes in collisions of O⁻ with atoms and molecules; mechanisms of one- and two-electron loss *J. Phys. B: At. Mol. Phys.* **20** 6065
- [134] Axford S D T and Hayhurst A N 1996 Mass spectrometric sampling of negative ions from flames of hydrogen and oxygen: the kinetics of electron attachment and detachment in hot mixtures of H₂O, O₂, OH and HO₂ *Proc. R. Soc. A* **452** 1007–33
- [135] Bortner M H and Baurer T 1978 *Defense Nuclear Agency Reaction Rate Handbook Second Revision Number 7* (Space Div., General Electric Co.)
- [136] Burkholder J B, Sander S P, Abbatt J P D, Barker J R, Huie R E, Kolb C E, Kurylo M J, Orkin V L, Wilmouth D M, and Wine P H 2015 Chemical kinetics and photochemical data for use in atmospheric studies: evaluation number 18 (Jet Propulsion Laboratory, National Aeronautics and Space Administration)
- [137] Pouvesle J M, Khacef A, Stevefelt J, Jahani H, Gyls V T and Collins C B 1988 Study of two-body and three-body channels for the reaction of metastable helium atoms with selected atomic and molecular species *J. Chem. Phys.* **88** 3061–71
- [138] Johnston H S 1968 Gas phase reaction kinetics of neutral oxygen species *Technical Report NSRDS-NBS-20* (National Bureau of Standards) (available at: <https://apps.dtic.mil/sti/citations/ADD095263>)
- [139] Slanger T G and Copeland R A 2003 Energetic oxygen in the upper atmosphere and the laboratory *Chem. Rev.* **103** 4731–66
- [140] Azyazov V N, Mikheyev P, Postell D and Heaven M C 2009 O₂(a¹Δ) quenching in the O/O₂/O₃ system *Chem. Phys. Lett.* **482** 56–61
- [141] Yan W and Economou D J 2016 Simulation of a non-equilibrium helium plasma bullet emerging into oxygen at high pressure (250–760 Torr) and interacting with a substrate *J. Appl. Phys.* **120** 123304